Pontifícia Universidade Católica
do Rio de Janeiro

Breno Perlingeiro Corrêa

Simulation and Analysis of SPDC-based Entangled Photon Pair Source for Quantum Communications with Spectral Multiplexing

Dissertação de Mestrado

Thesis presented to the Programa de Pós–graduação em Engenharia Elétrica, do Departamento de Engenharia Elétrica da PUC-Rio in partial fulfillment of the requirements for the degree of Mestre em Engenharia Elétrica.

Advisor: Prof. Gustavo Castro do Amaral

Rio de Janeiro
July 2022

PONTIFÍCIA UNIVERSIDADE CATÓLICA
DO RIO DE JANEIRO

Breno Perlingeiro Corrêa

Simulation and Analysis of SPDC-based Entangled Photon Pair Source for Quantum Communications with Spectral Multiplexing

Thesis presented to the Programa de Pós–graduação em Engenharia Elétrica da PUC-Rio in partial fulfillment of the requirements for the degree of Mestre em Engenharia Elétrica. Approved by the Examination Committee:

Prof. Gustavo Castro do Amaral
Advisor
Departamento de Engenharia Elétrica – PUC-Rio

Prof. Guilherme Penello Temporão
Departamento de Engenharia Elétrica – PUC-Rio

Dr. Bob Dirks
The Netherlands Organisation for Applied Scientific Research

Rio de Janeiro, July the 31st, 2022

Breno Perlingeiro Corrêa

Graduated in Electrical Engineering with an emphasis in telecommunications from the Pontifical Catholic University of Rio de Janeiro (Brazil). Member of the Laboratory of Optoelectronics since 2017 and one of the founding members of NuQuLO (Nucleus for Quantum Research in the Laboratory of Optoelectronics).

Bibliographic data

Corrêa, Breno Perlingeiro

Simulation and Analysis of SPDC-based Entangled Photon Pair Source for Quantum Communications with Spectral Multiplexing / Breno Perlingeiro Corrêa; advisor: Gustavo Castro do Amaral. – 2022.

83 f: il. color. ; 30 cm

Dissertação (mestrado) - Pontifícia Universidade Católica do Rio de Janeiro, Departamento de Engenharia Elétrica, 2022.

Inclui bibliografia

1. Electrical Engineering – Teses. 2. Fonte de Pares de Fótons Emaranhados. 3. Comunicação Quântica. 4. Redes Quânticas. 5. Repetidores Quânticos. I. Amaral, Gustavo. II. Pontifícia Universidade Católica do Rio de Janeiro. Departamento de Engenharia Elétrica. III. Título.

CDD: 621.3

To my mother, Patricia Perlingeiro and my girlfriend, Camila Lima.

Acknowledgments

I would like to first thank my grandparents, Jacir and Rosana, without whom I would not be here.

To my mother, Patricia Perlingeiro, for all her care, support, and guidance through all my life.

To my girlfriend, Camila Lima, for her affection, patience, and support.

To my advisor and friend, Gustavo Amaral, for his guidance, comprehension, support, magic games and shared knowledge.

To my colleagues and friends of PUC-Rio.

I would also like to thank the Brazilian agencies CNPq and FAPERJ for the financial support, which was crucial for this work realization.

This study was financed in part by the Coordenação de Aperfeiçoamento de Pessoal de Nível Superior - Brasil (CAPES) - Finance Code 001.

Abstract

Corrêa, Breno Perlingeiro; Amaral, Gustavo (Advisor). **Simulation and Analysis of SPDC-based Entangled Photon Pair Source for Quantum Communications with Spectral Multiplexing**. Rio de Janeiro, 2022. 83p. Dissertação de Mestrado – Departamento de Engenharia Elétrica, Pontifícia Universidade Católica do Rio de Janeiro.

The quantum internet has dragged the attention of many researchers and companies. The essential element to accomplish it is entanglement. Distributing entanglement allows the transmission of qubits without really sending them through the quantum channel. Therefore, the source that produces these entangled states shall do it reliably and with a competitive rate to classical communication. This work presents a simulation tool for the most common entangled photon pair source, the SPDC-based EPPS. Furthermore, using filters, we can emulate the effect of cavity-enhanced SPDC. Optimizing the parameters of the source, we achieved a 6dB gain on the Secret Key Rate compared to a simple SPDC process.

Keywords

Entangled Photon Pair Source; Quantum Communication; Quantum Network; Quantum Repeater.

Resumo

Corrêa, Breno Perlingeiro; Amaral, Gustavo. **Simulação e Análise de Fonte de Pares Emaranhados Baseada em SPDC para Comunicação Quantica com Multiplexação Espectral**. Rio de Janeiro, 2022. 83p. Dissertação de Mestrado – Departamento de Engenharia Elétrica, Pontifícia Universidade Católica do Rio de Janeiro.

A internet quântica atrai a atenção de muitos pesquisadores e empresas. O elemento essencial para realizá-la é o emaranhamento. A distribuição do emaranhamento permite a transmissão de qubits sem realmente enviá-los pelo canal quântico. Portanto, a fonte que produz esses estados emaranhados deve fazê-lo de forma confiável e com taxa competitiva à de comunicação clássica. Este trabalho apresenta uma ferramenta de simulação para a fonte de pares de fótons emaranhados mais comum, o EPPS baseado em SPDC. Além disso, usando filtros, emulamos o efeito do SPDC dentro de uma cavidade. Otimizando os parâmetros da fonte, obtivemos um ganho de 6dB na taxa de chaves secretas em comparação com um processo SPDC simples.

Palavras-chave

Fonte de Pares de Fótons Emaranhados; Comunicação Quântica; Redes Quânticas; Repetidores Quânticos.

Table of contents

List of figures

List of tables

List of Abreviations

EPPS – Entangled Photon Pair Source

SPDC – Spontaneous Parametric Down Conversion

BSM – Bell‘s State Measurement

PBS – Polarized Beam Splitter

BS – Beam Splitter

QKD – Quantum Key Distribution

QBER – Quantum Bit Error Rate

QR – Quantum Repeater

QM – Quantum Memory

AFC – Atomic Frequency Comb

JSA – Joint-Spectral Amplitude

JSI – Joint-Spectral Intensity

SVD – Singular Value Decomposition

ppLN – periodic poling Lithium Niobate

FWHM – Full Width at Half Maximum

"Science, my lad, is made up of mistakes, but they are mistakes which it is useful to make, because they lead little by little to the truth."

Jules Verne, *A Journey to the Center of the Earth.*

1 Introduction

At the beginning of the 20th century, the discovery and the studies of new physical phenomena culminated in a new branch of physics, so-called modern physics [1]. One of the products of this revolution is the theory called quantum mechanics, which, in summary, describes the nature of atomic and subatomic particles. As we shall see in the next chapter, this theory brings concepts that are contestants to our daily experience. At first glance, the statistical aspect of the measurements is intriguing. However, even if you accept it, there are other concepts even more mesmerizing [2].

Indeed, in the beginning, many physicists were trustless with quantum mechanics [3]. However, nowadays, researchers have proven most quantum mechanics predictions[4, 5]. Besides, we use many standard technologies developed using this theory inside every digital equipment, such as diodes, transistors, LEDs, and LASERs.

With the maturation of quantum mechanics at the end of the last century, scientists created the concept of quantum computers [6]. Devices capable of realizing computational operations on quantum states or bits, known as qubits. Therefore, quantum algorithms take advantage of quantum mechanics principles, for example, entanglement, one of the most fundamental tools. In short, two entangled states are quantum systems correlated at such a level that one cannot know which are the states individually, only by having information about both.

This concept allows quantum algorithms to optimize operations and then reduce the duration to accomplish tasks. One of the most famous examples is Shor's algorithm [7]. Peter Shor created it for quantum computers to find the prime factors of an integer number. This algorithm runs in polynomial time, while the fastest algorithm for classical computers runs in sub-exponential time. Shor's creation shows not only the promised superiority of the quantum computer but, as we shall see in section 1.3, threats to our privacy.

1.1 Distributed Quantum Computing and Quantum Teleportation

However, there is a gap between the theoretical and the practical quantum computer [8]. Quantum computers nowadays are limited by the number of qubits and the number of qubits that can interact. A way to overcome these limitations is to distribute the processing of the algorithms through different quantum processors, so-called distributed quantum computing [9, 10, 11, 12]. This idea consists of a net of quantum computers interconnected via a quantum channel transmitting qubit using quantum teleportation.

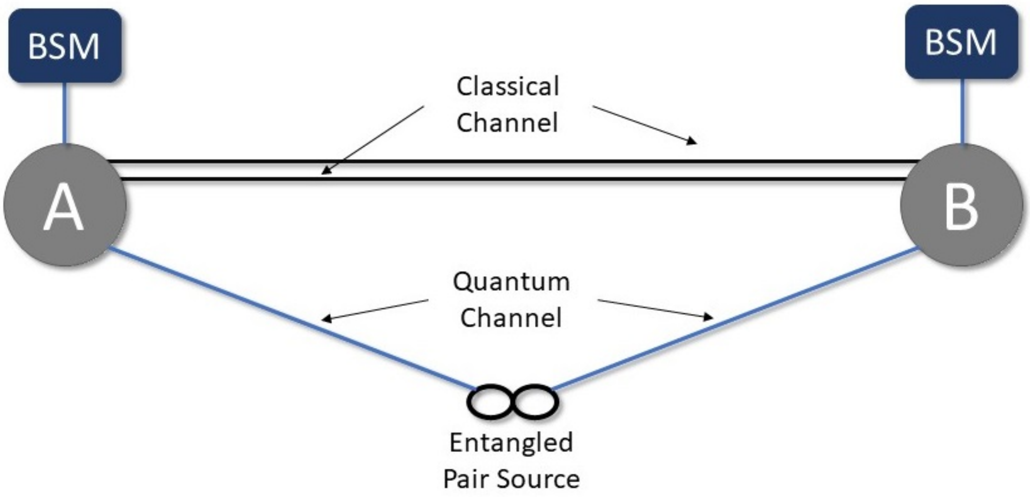

Figure 1.1: Sketch of a simple quantum teleport protocol, between two processors, A and B.

Quantum teleportation is an entangled-based protocol to share qubit or quantum states without the necessity of transmitting them through a channel [13]. Suppose two quantum processors are working together in an algorithm. A needs to send a resulting qubit of one of its operations to B. Between them, there is an entangled pair source, which produces and transmits a pair of entangled states, one to A and the other to B.

After receiving it, processor A will make a projective measure with the desired qubit and the entangled particle on the basis formed by the maximum entangled states. Since these states are called Bell's states, this measurement is called Bell's state measurement. After this process, A transmits through a two bits classical channel the result it got.

It is possible to demonstrate that after A's measurement, B holds a qubit, which is almost the one A wanted to transmit. The processor B needs to make a unitary transformation, which will depend on the result information A transmitted. Finally, after applying the right operation, B has the qubit that

A has sent and can continue the algorithm. The mathematical proof for this protocol is presented in chapter 2.

1.2 Quantum Network, Quantum Repeaters, and Entanglement Swapping

Besides overcoming the quantum computers' limitations, sharing entanglement with different processors arouses the idea of quantum networks [14, 15]. These networks would connect quantum computers and allow the users to exchange information. There is a long way for this occurs yet, however, researchers and companies are investigating the best technologies, protocols, and feasibility to make this happen [16, 17].

One of the most challenging obstacles for quantum internet is distance. Although the information does not have to travel through the quantum channel, the entangled states must pass. Commonly, these states are encoded in a degree of freedom of a photon, for example, polarization or time-bin. Photons are the predominant choice for long-distance transmissions due to their low loss and interaction with the environment compared to other particles [18].

However, even if using optical fibers and photons at telecommunications wavelength, the lowest attenuation factor is 0.2 dB per kilometer. Since we are working in a single-photon regime, this attenuation corresponds to the probability of a photon reaching the receiver. Therefore, considering a 400 km optical fiber link (approximately Rio-São Paulo), the rate of success is 1 in 10 million photons will achieve. In other words, if we use an entangled photon source with a pair generation rate of 100 MHz (which is a very high rate for an entangled photon source), the rate of photons in the receiver is 1 Hz [19].

In classical communications, the solutions for the attenuation issue are straightforward: increase the transmitter power or amplify the signal between Tx and Rx. Both of these are impractical for quantum communications. The transmitter is sending single photons, and enhancing the power means generating more photons, which would lead to a classical regime. Also, amplifiers would not solve the case since one cannot copy quantum states without adding noise, which is the principle of the no-cloning theorem [20].

How can we establish long distances communication using quantum channels? There is no definitive answer to questions yet, although the conceptual solution is well accepted. Before understanding how it works, let us reformulate the question: How can we distribute entangled states through long distances? As we saw in the quantum teleportation protocol: if two parties can share entanglement, they can send qubits. Moreover, we shall see other significant protocols which are more reliable.

The key to distributing entanglement through long distances is using entanglement swapping [21, 22]. The process is very similar to quantum teleportation, but instead of teleporting a simple state, we teleport an entangled state. For example, two parties, Alfred and Bruce, want to share entanglement, and they are at a distance of L from each other. Between them, there are two EPPS equally disposed. Each EPPS sends one photon to the closest node (A or B). The other component of the pair goes to a measuring station. This station performs a BSM with the incoming photons and then transmits the results to Alfred and Bruce. After receiving the answer of the measure, Alfred or Bruce applies a unitary transformation to their photon, so they share an entangled state. The reader finds the mathematical proof of this process in chapter 2.

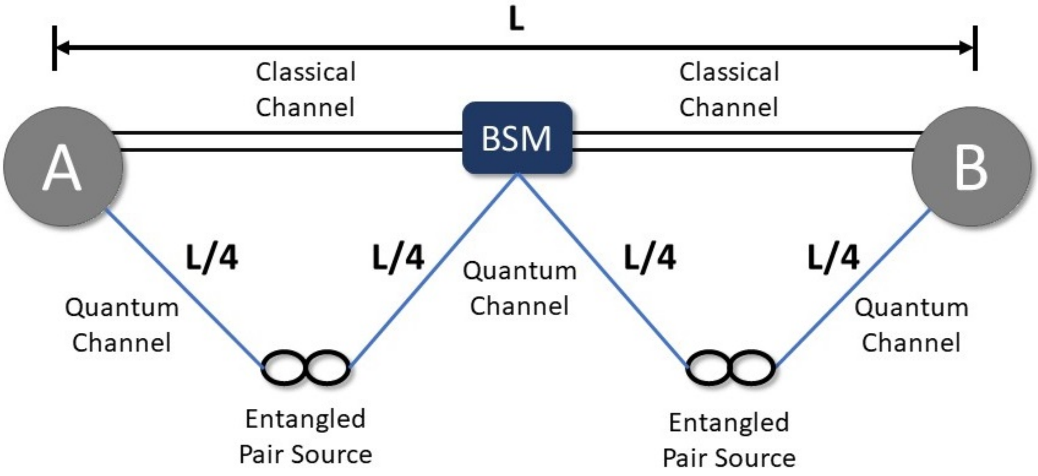

Figure 1.2: Illustration of the Entanglement Swapping between Alfred (represented by node A) and Bruce (represented by node B) described in the text. In this configuration, the EPPSs are equally distributed between A and B. This topology is commonly called quantum relay.

As we can see in the figure, the distance each photon shall pass is two times less than they would go through if it was the previous setup. Although, the chance of success would not change since A and B will share entangled states only if each photon reaches the nodes. Mathematically, considering only the attenuation, the probability of individual success is given by the Beer-Lambert law:

$$P_{L/4} = e^{-\alpha \frac{L}{4}} \tag{1-1}$$

Being L, the total distance between A and B, and alpha, the attenuation coefficient of a photon on an optical fiber. Since the four events are independent and the entanglement swapping success depends on the four photons hitting the endpoint, the probability is:

$$P_{\text{relay}}(S) = \left(P_{L/4}\right)^4 = \left(e^{-\alpha\,\frac{L}{4}}\right)^4 = e^{-\alpha\,L} \tag{1-2}$$

Therefore, the result is the same for direct transmission and the scheme depicted in figure 1.1. Actually, if we consider the efficiency of the BSM, the success chance reduces, making this configuration even worse than the ones cited before. However, if one could store the successfully transmitted states, it would free the process from the dependence on the simultaneous success of each transmission. Indeed, there is a device capable of doing this task, quantum memory (QM).

There are different types of quantum memories, each with its peculiarity. In general, these devices receive a photon, annihilate it, but hold its quantum state. After a while, they emit a photon with the stored state. For some memories, the storage time is fixed, and others are on-demand, for example, memories based on trapped rubidium atoms and Atomic frequency Comb memories, respectively. Because each memory has there advantages and disadvantages, one cannot select which is the best. However, the variety allows the users to choose which memory fits best according to their requirements [23, 17].

To improve the topology presented in figure 1.2, Alfred and Bruce (A and B, respectively) should have a quantum memory and the BSM station, two: one for each incoming photon. After this alteration, the BSM station will only measure after all the memories are filled. Consequently, the success of the entanglement swapping does not depend on the photons arriving simultaneously on the nodes [24]. This topology is the way to overcome the long-distance issue and is well-known as the quantum repeater [25, 26, 19, 27, 28].

To calculate the probability of successfully distributing entanglement for the quantum repeater, we shall look at the situation from a different perspective. First, what is the probability of none or only of the entangled pairs getting to the memory? It is one minus the probability of all pairs getting into their memories. Therefore, it is one minus the probability of success for the quantum relay (see equation 1-2). Besides, for generality, we shall consider the efficiency of the BSM, so the expression is the following.

$$1 - \eta_{BSM}\,P_{\text{relay}}(F) = 1 - \eta_{BSM}\,e^{-\alpha\,L} \tag{1-3}$$

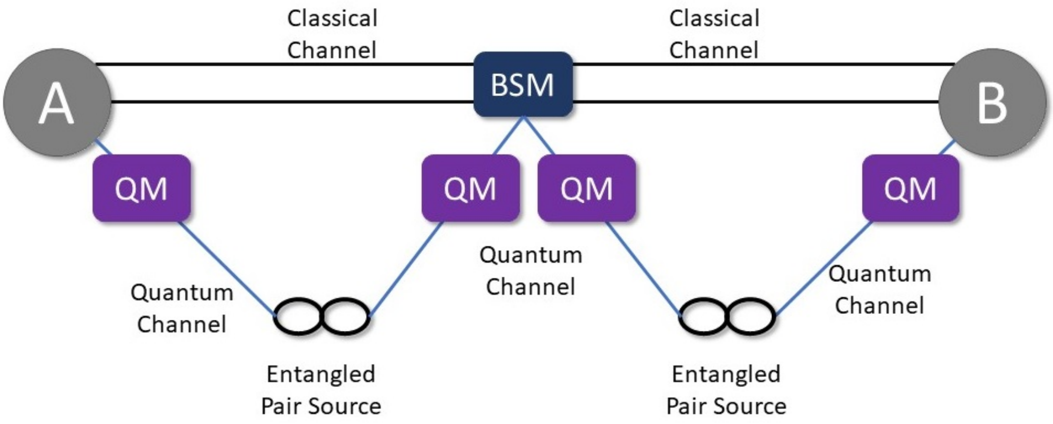

Figure 1.3: Illustration of the Entanglement Swapping between Alfred (represented by node A) and Bruce (represented by node B) using quantum memories. These topology is well-known as quantum repeater.

Since, in this case, we have quantum memories, we can store successfully transmitted states on them and try again the ones that went wrong. Therefore, the probability of failure ($P_{QR}(F)$) is the chance of getting no pairs distributed or only one in all the attempts. Due to the independence of the events, $P_{QR}(F)$ is:

$$P_{QR}(F) = (1 - \eta_{BSM}\, P_{\text{relay}})^N = \left(1 - \eta_{BSM}\, e^{-\alpha\, L}\right)^N \tag{1-4}$$

N is the number of attempts or, more rigorously, the number of modes. For simplicity's sake, let us consider temporal modes. The quantum memory can receive photons for a window of time τ, and the EPPS generates pairs with a certain rate R. Therefore, the number of modes (N) is $\tau \times R$ for this case. Since time and frequency are Fourier pairs, one can also use spectral modes.

With the expression for the likelihood of failing, it is easy to obtain the success probability, since these events are complements.

$$P_{QR}(S) = 1 - P_{QR}(F) = 1 - \left(1 - \eta_{BSM}\, e^{-\alpha\, L}\right)^N \tag{1-5}$$

To understand the magnitude of the quantum repeater, we shall compare its efficiency to the quantum relay and direct transmission. Before, we have to make some assumptions: the attenuation coefficient is 0.2 dB/m (for a 1550 nm photon in optical fibers) [29], and the BSM efficiency is 0.5, which is the maximum possible [30]. Figure 1.4 illustrates this comparison, plotting the probability of success for a direct link, a quantum relay, and quantum repeaters with 2, 5, and 10 modes.

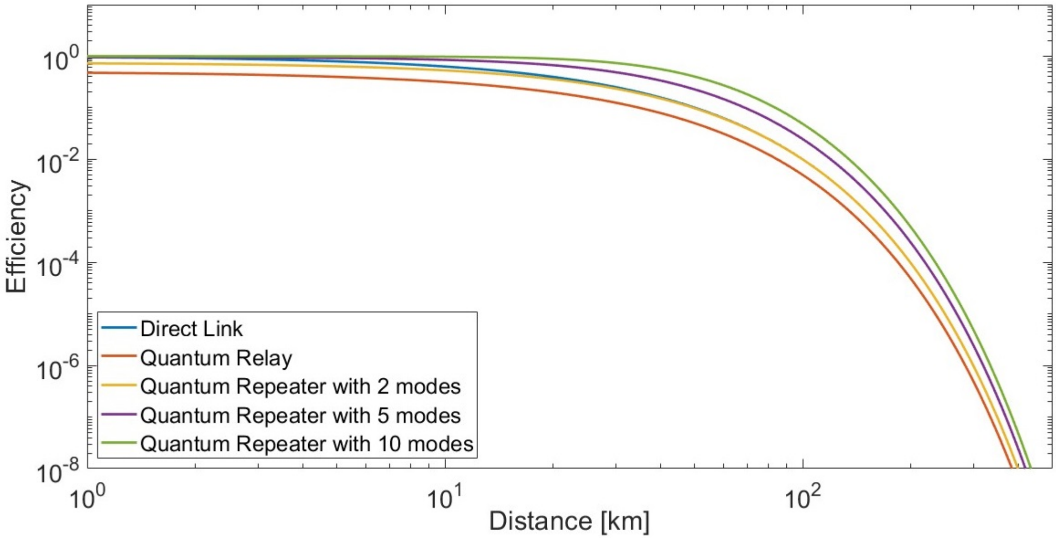

Figure 1.4: Plot of the efficiency for different configurations of link. Assuming the attenuation coefficient of 0.2 dB/km (≈ 0.046 Np/km) and the Bell's state measurement efficiency, 0.5.

As expected, the quantum relay has the worst performance due to the BSM insertion. Although the two-mode quantum repeater configuration is also inferior to straightforward communication, as the number of modes increases, the quantum repeater performs better on long distances. Therefore, we prove the superiority of this setup and that it can solve the long-distance problem.

Moreover, one can concatenate quantum repeaters to achieve even further distances. We shall consider the two EPPS and the BSM station with two memories an elementary link. Thus, one could copy and interconnect these links, as illustrated in figure 1.5.

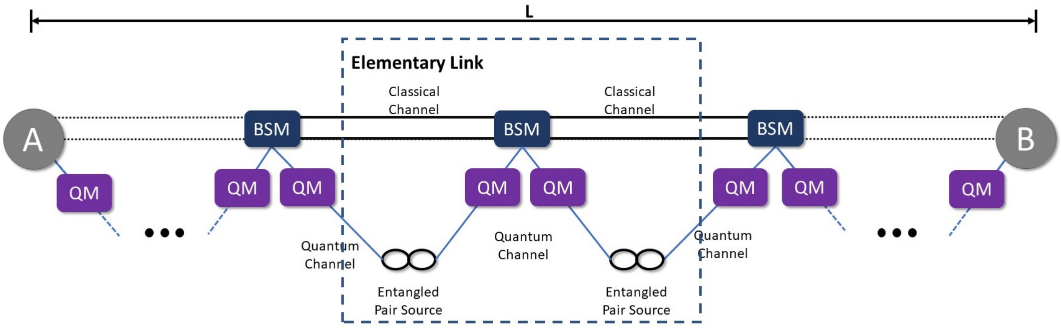

Figure 1.5: Concatenation of N elementary links of quantum repeaters between Alfred (represented by node A) and Bruce (represented by the node B).

Therefore, the quantum repeater topology is a promise for the physical layer of the quantum networks because it allows the distribution of entanglement and overcomes the direct transmission efficiency. Henceforth, we shall see one of the many applications one can do with shared entangled states.

Ultimately, we shall discuss the focus of this dissertation, which is an element present in all schemes and structures we have seen.

1.3 Quantum Key Distribution and BBM92

As discussed before, quantum computers, theoretically, can overcome the processing time of classical computers [31, 32]. Thus, this will be an essential tool for future calculations and simulations of our world [33]. On the other hand, this is a threat to currently cyber safety [34, 35]. The RSA is the most refined and reliable cryptography protocol for classical computers. In short, this encryption bases its security on the fact that does not exist efficient algorithm to factor large integers. In other words, it can take centuries to decompose the integers and obtain the secret key, which encodes the messages.

However, in 1994, Peter Shor developed an algorithm for quantum computers capable of factoring integers in a polynomial time, while the best classical method scales exponentially [7]. Nowadays, does not exist quantum computers able to break the RSA encryption due to the necessity of a large number of qubits. But, it is a question of time for it to achieve this since the investment in this technology increases year by year [36, 37].

The quantum threat, the name given to this information safety threat that the quantum computation represents, arouses the discussion about reliable communication. In 1984, Charles Bennett and Gilles Brassard developed the first cryptography protocol based on quantum mechanics, the so-called BB84 [38]. Although it was not their purpose (since it was ten years before Peter Shor came up with the algorithm to factor integers), this first protocol and the ones sequenced are the solutions to the quantum threat [39].

The BB84 is the founder of the quantum key distribution (QKD). After this, other protocols emerged. All of them inherited something from BB84, which consists of two parties, Alice and Bob, producing and sharing a secret random key through a quantum channel. Hence, one of the parties encrypts the information using the shared key and sends it to the other through a classical channel. Then, the receiver decodes the message and recovers the information. To answer, they share another secret key and do the process again, similar to the one-time pad protocol.

The security essence of QKD is associated with the no-cloning The security essence of QKD is associated with the no-cloning theorem, which infers that one cannot copy or amplify quantum states without introducing noise [20]. For example, if an eavesdropper (so-called Eve) steals qubits from the secret keys and tries to send copies of them to pass unnoticed. However, she will introduce noise (this attack is one the most straightforward and is called intercept and resend). In other words, the qubit error rate (QBER) will increase. Henceforth, researchers calculated a maximum QBER of 11%, which indicates the limit where Eve has less information about the keys than the receiver [40].

Moreover, the setup presented before, the quantum repeater, allows the utilization of QKD to communicate. But they have to use an entangled-based QKD since the design of quantum repeater is for entanglement distribution. In other words, Alice or Bob do not have to prepare and send states, but they have to share entangled states.

After the BB84, in 1991, Arthur Ekert developed the first entangled-based QKD protocol, popularly called E91 [41]. The protocol bases its reliability on violating locality, in other words, overcoming the Bell's limit for local measurements. One year after, the authors of BB84 with David Mermin (BBM92) proposed a new entangled-based QKD without Bell's theorem [42]. The security of BBM92 relies on the decomposition of the protocol into the BB84.

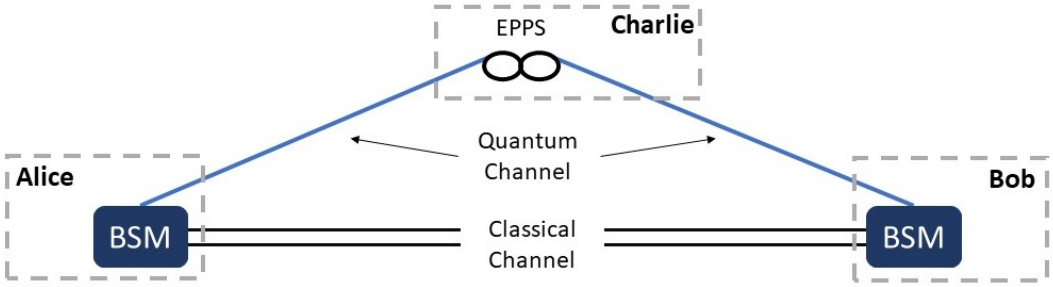

Figure 1.6: Simple scheme for a BBM92 protocol.

The figure1.6 presents a block diagram for the BBM92 protocol. The premise is that Alice and Bob want to send information safely. To facilitate the comprehension, let us consider a third party called Charlie, responsible for generating and sending the entangled photons. On the other hand, Alice and Bob receive these photons and perform a Bell's states measurement.

Without entering into the mathematics of quantum mechanics (which you can find in the next chapter), we shall understand the concept behind the BSM of a single photon. Without losing generality, let us consider that the qubits are encoded on the polarization state of the photons. Before the communication, Alice and Bob must agree on two polarization basis. The standard ones are the rectilinear and the diagonal basis. Besides, They must know which entangled state Charlie will be sending them.

After this preparation, Charlie starts sending photons. Alice and Bob randomly choose one of the accorded basis to measure the incoming photon. Both save their results and the basis for each. These steps configure the way of implementing a BSM for polarization encoded photons.

Thus, Alice and Bob start the sifting step. They communicate via a public classical channel, the basis they used for each measurement. Then, they discard the result in which the bases are mismatched. Therefore, on average, they now have half of the transmitted key, known as the sifted key. Now, the two parties can sacrifice a part of the key to measure the error rate and verify the reliability of the channel.

Finally, Alice and Bob have their secret key. Depending on the state prepared by Charlie, one of the parties has to apply a bit of flip. Further, they can implement error correction codes or make privacy amplification to improve the robustness of the process [43, 44]. Thus, they can encrypt their information and share it on a classical. Notice that the message must have the same length as the key. Also, the protocol inherits from the one-time pad that the secret key can be used by the parties once. Therefore, for each transmission, they have to establish a new key.

Although QKD protocols are secure proof from quantum computers, the performance of the processes and technologies for implementing them are not high enough compared to classical communication [45]. The same happens for the quantum repeater [46]. Therefore, some research groups and companies aim to enhance the performance of these elements to make these technologies marketable. This work intends to simulate and analyze one of the most typical elements of quantum repeaters and entangled-based QKD, the entangled photon-pair source based on spontaneous parametric down-conversion.

1.4 Entangled Photon Pair Sources and The SPDC

All the schemes seen before have at least one entangled photon-pair source since, to distribute entanglement, one must have a source of such states. This element is crucial for the future of quantum communications. Even if one has the most efficient and reliable quantum memory, although the states stored are not entangled or not near one of the Bell states, one cannot implement entanglement swapping. The same for the entangled-based QKD. The protocol reliability depends on the fact that the qubits are not separable and correlated.

Consequently, it is essential for quantum communication the studies and improvements on EPPSs. There are many methods of generating entangled photons, the pioneer and most common is the EPPS based on spontaneous parametric down-conversion, for short SPDC. This process occurs in non-linear mediums when a photon spontaneously interacts with itself due to the medium characteristics. Then, it converts itself into two photons of lower energy (down-conversion). And, since the process does not change the attributes of the material, it is parametric [47, 48].

Although SPDC is the most typical method, it does not have the best performance compared, for example, to quantum dots or Nitrogen vacancy on diamonds. Indeed, the SPDC is not an efficient process, as we shall see in the next chapter [49, 50]. However, SPDC does not demand cryogenic temperatures or highly prepared materials [51]. In summary, to assemble an SPDC, one needs a pulsed laser and a periodic poled non-linear crystal. Since this technology has more than 20 years, the confection of this crystal is very mature, and there are even corporations selling EPPS based on SPDC [52, 53].

Due to these facilities, it is interesting for researchers and companies to improve the SPDC method. The main idea is to maintain the simple implementation and make its performance competitive with the other process of generating entangled photons pairs. One of the methods for enhancing the efficiency of the SPDC is using filters or, even better, putting the crystal inside a cavity, then producing entangled pairs frequency multiplexed [54, 55].

In this work, we shall implement simulations of an SPDC-based entangled photon source and take some parameters of this source as figures of merits for the analysis. Such parameters are spectral purity, second-order cross-correlation, qubit error rate (QBER), and secure key rate [56]. In chapter 2, the reader finds an overview of quantum mechanics and other concepts. Then, in chapter 3, we shall understand the SPDC process. Chapter 4 presents the simulation results and the analysis.

2
Theoretical Background

This chapter lays the foundations for the comprehension of spontaneous parametric down-conversion. It starts with an introduction to quantum mechanics, enunciating and explaining its postulates. Then, using the quantum approach, we shall see the harmonic oscillator. Elevating this, we will study a system with two particles and learn about entanglement. With this knowledge, we can examine the math around quantum teleportation and entanglement swapping.

2.1
Postulates of quantum mechanics

Quantum mechanics is an extensive theory in physics responsible for describing systems on an atomic scale. There are some postulates which provide a mathematical approach for describing the phenomena. The number of postulates and the order of enunciating them differs from book to book, but overall, they get to the same point. Here we shall use [2] as a reference since it is more detailed.

The first postulate enunciates that the state of a physical system can be represented as a complex vector, a state vector, which belongs to a Hilbert space, well known as a space state. It is relevant to notice that the state space and the state vector are something to determine. Using Dirac's notation, an arbitrary state can be $|\psi(t)\rangle$.

The second postulate enunciates that every measurable physical quantity can be represented as an observable operator acting in the system's associated Hilbert space. Following this, the third postulate affirms that the only measurable results are the eigenvalues of the observable operator related to the measurement. For example, consider an arbitrary measurement, represented by an observable $\hat{A}$ applied to a particle described in one of their eigenstates, $|u_n\rangle$. The only possible result is the related eigenvalue, a_n.

$$\hat{A}\,|u_n\rangle = a_n\,|u_n\rangle \tag{2-1}$$

What if the particle's state was not the eigenstate of $\hat{A}$? The Fourth postulate enunciates that the probability of measuring a specific eigenvalue of an observable is equal to the square module of the projection coefficient of the current state in the correspondent eigenstate. The following equation exemplifies the probability for a non-degenerated case.

$$P(a_n) = | \langle u_n|\psi\rangle |^2 \tag{2-2}$$

The fifth postulate affirms that immediately after being measured, the particle collapses to the projection of the initial state on the eigenstate related to the measured eigenvalue. Following the previous example, the particle's state immediately after measuring a_n, $|\psi'\rangle$, is represented by equation 2-3, where P_n is the projection operator on state $|u_n\rangle$.

$$|\psi'\rangle = \frac{|u_n\rangle \langle u_n|\psi\rangle}{\sqrt{| \langle u_n|\psi\rangle |^2}} = \frac{P_n |\psi\rangle}{\sqrt{\langle\psi| P_n |\psi\rangle}} \tag{2-3}$$

Finally, the sixth postulate enunciates that the time evolution of state $|\psi(t)\rangle$ is ruled by the Schrödinger equation, as shown in 2-4. Where $\hat{H}(t)$ is the Hamiltonian operator, an observable associated with the system's total energy. One can obtain it from the classical Hamiltonian.

$$i\hbar\frac{d}{dt} |\psi(t)\rangle = \hat{H}(t) |\psi(t)\rangle \tag{2-4}$$

If the Hamiltonian is time-independent, one can simplify the expression above to 2-5. Otherwise, it is necessary to use methods for solving differential equations.

$$|\psi(t)\rangle = e^{-\frac{i\hat{H}}{\hbar}} |\psi(t)\rangle \tag{2-5}$$

This mathematical formalism of this section provides us tools to investigate an essential classical system, the harmonic oscillator, but in light of quantum mechanics. Furthermore, we shall extend this knowledge to understand entanglement.

2.2 The Harmonic Oscillator and Fock States

Consider a simple, but essential case, an electromagnetic field confined in a one-dimensional cavity. After doing some classical analysis, the Hamiltonian for this system is obtained [57]. The equation 2-6 presents it, where $\hat{p}$ and $\hat{q}$ are the momentum and position operators, respectively. Both are Hermitian, consequently observables.

$$\hat{H} = \frac{1}{2}\left(\hat{p}^2 + \omega^2\hat{q}^2\right) \tag{2-6}$$

A more convenient approach is using two non-observable operators, well known as annihilation and creation operators (2-7 and 2-8, respectively). These two provide a more straightforward method to find the allowed energies and their related states.

$$\hat{a} = (2\hbar\omega)^{-1/2}(\omega\hat{q} + i\hat{p}) \tag{2-7}$$

$$\hat{a}^{\dagger} = (2\hbar\omega)^{-1/2}(\omega\hat{q} - i\hat{p}) \tag{2-8}$$

Rewriting the Hamiltonian in terms of $\hat{a}$ and $\hat{a}^{\dagger}$:

$$\hat{H} = \hbar\omega\left(\hat{a}^{\dagger}\hat{a} + \frac{1}{2}\right) \tag{2-9}$$

The product $\hat{a}^{\dagger}\hat{a}$ has a relevant purpose, so-called number operator, $\hat{n}$. We denote its eigenstates as $|n\rangle$, consequently the eigenstates of the Hamiltonian. A physical interpretation is that it corresponds to a state of a well-defined number of photons inside the cavity, well-known as Fock state. Each of these states has an energy associated E_n, eigenvalue of $\hat{H}$. Hence, we shall see the effect of applying the creation operator with the Hamiltonian, to understand their purpose [57].

$$\hat{H}(\hat{a}^{\dagger}|n\rangle) = (E_n + \hbar\omega)(\hat{a}^{\dagger}|n\rangle) \tag{2-10}$$

$$\hat{H}(\hat{a}|n\rangle) = (E_n - \hbar\omega)(\hat{a}|n\rangle) \tag{2-11}$$

From now on, we understand the name of the operators $\hat{a}^{\dagger}$ and $\hat{a}$. The creation operator enhances the system's energy by $\hbar\omega$, therefore increasing one photon of frequency ω. On the other side, the annihilation operator exterminates a photon of energy $\hbar\omega$. Attaching this to the Fock state, we get to equations 2-12 and 2-13.

$$\hat{a}|n\rangle = \sqrt{n}\,|n-1\rangle \tag{2-12}$$

$$\hat{a}^{\dagger}|n\rangle = \sqrt{nthe+1}\,|n+1\rangle \tag{2-13}$$

Finally, we shall find the allowed energy values, E_n:

$$E_n = \langle n|\,\hat{H}\,|n\rangle = \hbar\omega\left(n + \frac{1}{2}\right) \tag{2-14}$$

We shall remark on the single-mode field analysis' fascinating points. The Fock states form an orthogonal complete set, serving as a basis for well-known photon systems. The multimode field is naturally obtained since the problem can be reduced into "M" single-mode fields, where "M" is the number of modes. The last one is the most intriguing fact, the zero-point energy (ZPE). Following the equation 2-14, the case without photons ($n = 0$) has energy equal to $\hbar\omega/2$. This fact gives rise to two other effects: Lamb Shift and the Casimir effect [57].

The quantum solution for the harmonic oscillator provides the notation to describe the SPDC process. Since the system is composed of two states,

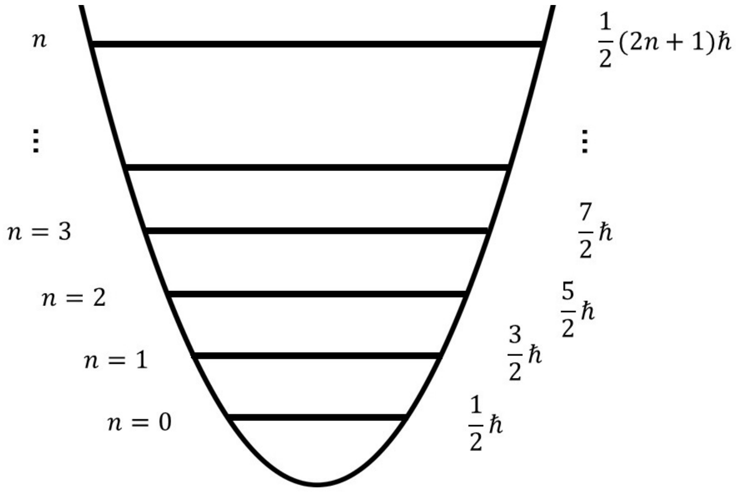

Figure 2.1: The energy levels of an arbitrary harmonic oscillator.

there is a representation we shall study before the analysis. This description allows us to write joint and incompletely known states. Finally, it leads us to quantum entanglement.

2.3 Pure and mixed states

Initially, in this chapter, well-defined states were adopted to represent quantum systems. However, if the state, in which the system is, is indistinguishable, this nomenclature is inadequate. Then, the density operator or density matrix emerges as a representation of these states. Suppose a quantum system has probabilities p_i of being in the $|\psi_i\rangle$ states, the density operator is defined:

$$\rho \equiv \sum_i p_i \left|\psi_i\right\rangle \left\langle\psi_i\right| \tag{2-15}$$

This tool provides the characterization of states into pure, the well-defined ones, and mixed, probability combination of pure states. In summarizing, since the system can be represented as a state vector, it is called pure. Otherwise, the exclusive representation is the density operator, then is called mixed. A numerical way to define is by calculating the purity of the state, which is given by the following.

$$P(\rho) = \sum_i p_i^2 = Tr(\rho^2) \tag{2-16}$$

If the purity is 1, then is a pure state. Otherwise, if it is less than 1, the state is mixed.

2.4 Systems with two or more particles and Entanglement

Now, introducing the knowledge of systems with two or more particles. Since it is a vector space, the state-space of a composite system is the tensor product of the component systems [2]. Therefore, if there are N particles, each in $|\psi_i\rangle$, the resulting space state is: $|\psi_1\rangle \otimes |\psi_2\rangle \otimes .. \otimes |\psi_N\rangle$. A common representation for composite systems is using one ket with the states inside. For example, a two particles system, $|\psi_1\rangle \otimes |\psi_2\rangle$, it would be represented like $|\psi_1\psi_2\rangle$.

If the joint state cannot be decomposed into pure states, the only solution is to use the density operator. To obtain the reduced density operator, we must do the partial trace of the matrix over the undesired system. Moreover, these joint states which cannot be written into a tensor product of pure states are called entangled.

As we have seen in the last chapter, entanglement is essential to quantum communication and quantum computation. We shall analyze an example to understand some of its implications. First, we define a two-eigenstates system, like polarization, spin, or time-bin. Associated with these states are often used a computational representation, so-called Qubit: $|0\rangle$ and $|1\rangle$. Now, consider the following states composed of two Qubits:

$$|\Phi^+\rangle = \frac{1}{\sqrt{2}}|11\rangle + \frac{1}{\sqrt{2}}|00\rangle \tag{2-17}$$

Suppose that the state $|1\rangle$ measurement results in 1, on other hand, $|0\rangle$ results in -1. If we separate the particles and send one to Alice and the other to Bob, the first to perform a measure knows exactly the other's result. In other words, if Alice measures first and gets 1, she knows exactly that Bob will obtain the same result.

This state is called $|\Phi^+\rangle$ and it constitutes the Bell States, which are the maximum entangled states. The other three states that constitute the set of Bell states are:

$$|\Phi^-\rangle = \frac{1}{\sqrt{2}}|00\rangle - \frac{1}{\sqrt{2}}|11\rangle \tag{2-18}$$

$$|\Psi^+\rangle = \frac{1}{\sqrt{2}}|01\rangle + \frac{1}{\sqrt{2}}|10\rangle \tag{2-19}$$

$$|\Psi^-\rangle = \frac{1}{\sqrt{2}}|01\rangle - \frac{1}{\sqrt{2}}|10\rangle \tag{2-20}$$

Using the inner product note that these states are orthogonal to each other and have norm 1. Therefore, this set forms an orthonormal basis for the bipartite space state. Besides, using the density matrix approach, one can notice that the Bell states are pure (purity equals 1). However, if one tries to split into two density matrices, using the partial trace, it results in two maximum mixed states ($I/2$). Consequently, we verify that one only knows the state, if one has information about both states, otherwise it is just a mixed state, and the statistical result is always 50% for every measuring basis.

Indeed, entanglement is so unnatural for our daily experience that one of the most brilliant minds of the 20th century, Albert Einstein, in collaboration with Nathan Rosen and Boris Podolsky, used it as an argument to prove that quantum mechanics is incomplete [3]. The EPR paradox suggested that this strange effect (entanglement was not named yet) violates local realism.

However, we know, until nowadays, that the quantum theory describes nature's microscopic systems. Besides, entanglement is a feasible and measurable effect. And the proof of it came with the so-called Bell's inequality.

The easiest way to understand this proof is by example. Suppose two particles are generated and transmitted one to Alice and the other to Bob. She is capable of measuring two properties that this particle has P_Q and P_R, which results in a value Q and R, respectively. Bob also can measure two properties P_S and P_T, which results in a value S and T, respectively. Q, R, S, and T can assume values of 1 or -1.

Both randomly choose one of the possible projections and perform them at the same time. After a large number of measures, the locality of this system is examined by the following inequality:

$$E[QS] + E[RT] + E[RS] - E[QT] \leq 2\,, \tag{2-21}$$

where $E[\cdot]$ represents the expected value of the term. This result is also called CHSH after the initials of its four discoverers [58]. It is a specific component of a set of inequalities so-called Bell's inequalities. Therefore, systems that attend the local realism accord to 2-21. However, for perfect entangled pairs, this calculus leads to $2\sqrt{2}$. Indeed, experiments show that local realism violated [59]. are There are still open metaphysical discussions about realism and the completeness of quantum mechanics and more, because of that. However, it also gives us a powerful tool for quantum communication, entanglement. Henceforth, we shall see the mathematical approach behind protocols seen in the introduction, quantum teleportation, and entanglement swapping.

2.5 Quantum Teleportation and Entanglement Swapping

In the introduction, we examined the use of entanglement as a tool for communication. Then, we discussed two protocols, quantum teleportation, and entanglement swapping. Here, we shall utilize the mathematical approach for quantum mechanics to prove the functionality of these protocols.

First, we shall understand quantum teleportation since entanglement swapping uses the same procedures but is more complex. Consider the scheme in figure 1.1, and Alfred (represented by A) wants to send a qubit to Bruce (represented by B). Between them, there is an entangled photon source, which sends one entangled photon to Alfred and the other to Bruce. Without loss of generality, consider that this source produces the state Ψ^+.

Alfred's state is:

$$|a\rangle = \alpha |0\rangle + \beta |1\rangle \tag{2-22}$$

Where α and β belongs to the complex plane, and such that $| \langle a|a\rangle |^2 = 1$. Then, after Alfred has received the entangled state, the total system state is:

$$|\Psi_{total}\rangle = |a\rangle_a \bigotimes |Psi^+\rangle_{AB} \tag{2-23}$$

Where the subscript denotes to which space that state belongs. One can expand this expression and reorganize it to:

$$\begin{aligned} |\Psi_{total}\rangle = \frac{1}{2}[\, &|\Phi^+\rangle_{aA} \bigotimes (\beta |0\rangle_B + \alpha |1\rangle_B) - \\ &|\Phi^-\rangle_{aA} \bigotimes (\beta |0\rangle_B - \alpha |1\rangle_B) + \\ &|\Psi^+\rangle_{aA} \bigotimes (\alpha |0\rangle_B + \beta |1\rangle_B) - \\ &|\Psi^-\rangle_{aA} \bigotimes (\alpha |0\rangle_B - \beta |1\rangle_B)] \end{aligned} \tag{2-24}$$

Alfred performs a Bell state measurement on the received entangled state and the state he wants to send Bruce. Using the reorganized equation (2-24), one can notice that there is a 25% chance of Alfred measuring $|Psi^+\rangle$ and Bruce gets the state $|a\rangle$. But the other results are almost that state, Bruce has to apply one of the Pauli operators on the receiving qubit. Therefore, Alfred transmits through a classical channel to Bruce, which of the Bells states he measured. Then, Bruce knows which operation he has to do to obtain $|a\rangle$ [60].

Noteworthy, if the state sent to Alfred and Bruce is another Bell state, the only difference would be the operation that Bruce has to apply to obtain the qubit Alfred wants to send. Besides, suppose that Alfred was intermediating this message, and he has just to deliver it to Bruce. Using the quantum teleportation protocol, Alfred does not have access to the information [57].

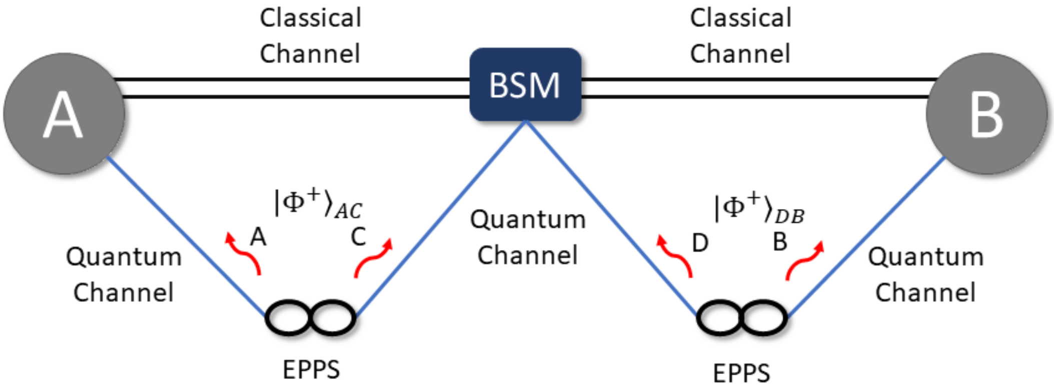

Figure 2.2: Scheme of an Entanglement Swapping protocol between A and B, assuming the sources produce the state $|\Phi^+\rangle$. For better understanding, the photon going to A and B are represented by their letters and the ones that go to the BSM are C and D.

Now, consider the scheme illustrated in figure 2.2, and Alfred and Bruce want to share entanglement. Without loss of generality, suppose that the sources produce the state $|\Phi^+\rangle$. The states going to Alfred and Bruce are denoted by the letter A and B, respectively. The others are C and D, where C is entangled with A and D with B. Therefore the total state for this case is:

$$|\Psi_{total}\rangle = |\Phi^+\rangle_{AC} \bigotimes |\Phi^+\rangle_{BD} \tag{2-25}$$

Where the subscript denotes to which bipartite space that state belongs. Similar to the quantum teleportation protocol, one can expand this expression and reorganize it to:

$$\begin{aligned}|\Psi_{total}\rangle = \frac{1}{2}[\,&|\Phi^+\rangle_{CD} \bigotimes |\Phi^+\rangle_{AB} + |\Phi^-\rangle_{CD} \bigotimes |\Phi^-\rangle_{AB} + \\ &+ |\Psi^+\rangle_{CD} \bigotimes |\Psi^+\rangle_{AB} + |\Psi^-\rangle_{CD} \bigotimes |\Psi^-\rangle_{AB}]\end{aligned} \tag{2-26}$$

After reorganizing the state, it is easy to see that after measuring C and D, on the Bells states basis, A and B are entangled. However, Alfred and Bruce must know which is their state. Therefore, the BSM station transmits the result through a classical channel. If the initials entangled states were different, the only thing that would change is the correspondence of the resulting measurement and entangled state.

These calculations consider that the sources always produce maximally entangled states, which is not in accord with the practice. There are parameters associated with the source that represents how close to the Bells states are the generated pairs. Henceforth, we shall understand the theory behind the SPDC, the parameter that characterizes an EPPS, and which characteristics of the SPDC are related to them.

3
Spontaneous Parametric Down Conversion

In this chapter, we shall study the theory behind spontaneous parametric down-conversion. First, we have a brief introduction to nonlinear optics and the classical process of three-wave-mixing, which is the opposite of SPDC. Then, we apply the quantum mechanics and mathematical concepts seen in the last chapter to write the SPDC Hamiltonian and resulting state. Hence, we shall study some figures of merit to characterize and evaluate the performance of the source.

3.1
Nonlinear Optics and Three-Wave-Mixing

An electric field, applied in a medium, polarizes the molecules generating dipoles in the opposite direction. The dipole per unit volume or polarization ($P(t)$) depends on the electric field amplitude ($E(t)$) and medium parameters [61].

$$P(t) = \epsilon_0 \left[\chi^{(1)}E(t) + \chi^{(2)}E^2(t) + \chi^{(3)}E^3(t) + ...\right] \tag{3-1}$$

The $\chi^{(i)}$ represents the susceptibilities of the material, and the "i" is the order of it. If the electric field strength is low, just the order one susceptibility is considered. As the intensity increases, higher-order terms become more relevant. Consequently, the nonlinear effect arises. The order depends on the material's crystal structure, particularly on its symmetry. The second-order term is fundamental for the parametric down-conversion process. Therefore, the crystal choice is restricted to mediums with a high second-order parameter, like Lithium Niobate or Potassium Titanyl Phosphate.

Moreover, an essential discussion in nonlinear optics is the phase-matching condition. This parameter is related to the momentum conservation of the process, and also to the efficiency of the process.

Consider three electromagnetic waves propagating through a nonlinear crystal, with frequencies ω_p, ω_s, ω_i and wave-vectors k_p, k_s and k_i, where p, s and i stand for pump, signal, and idler, respectively. In this case, the phase mismatch follows the expression 3-2. Mathematically, the phase mismatch (Δk)

appears in the output's intensity, in a square sine cardinal (Sinc) function, so this is optimized when $\Delta k = 0$.

$$\Delta k = k_p - k_s - k_i \tag{3-2}$$

The material's birefringence is essential to achieving the phase-matching condition. However, there are crystals, for which this parameter is not sufficient. So, the solution is a technique called quasi-phase-matching. It consists of using periodically poled crystals to obtain $\Delta k = 0$. This material had its structure engineered in such a manner that the orientation of one of the crystalline axes is inverted periodically. The periodic alternation complements the Δk to make it zero. Back to the previous example, using a periodically poled crystal the QPM equation is:

$$\Delta k = k_p - k_s - k_i - \frac{2\pi}{\Lambda}\,, \tag{3-3}$$

where Λ is the polling period.

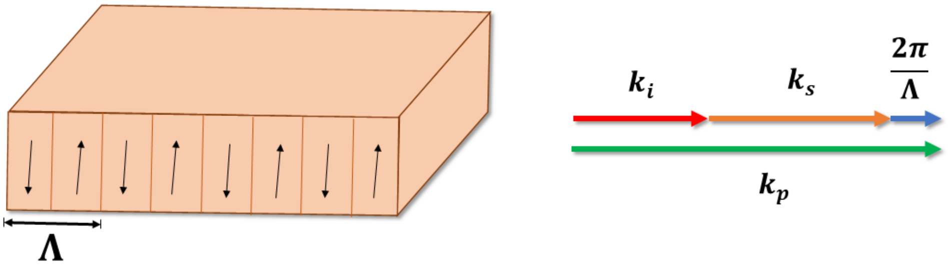

Figure 3.1: Illustration of the periodically poled crystal and the momentum conservation with the Quasi-Phase-Matching.

Classically, there is a nonlinear optical process called three-wave-mixing, in which two beams (ω_1 and ω_2) focused on a crystal generate a third beam (ω_3) with the sum of frequencies ($\omega_3 = \omega_1 + \omega_2$). The intensity of the generated beam is:

$$I_3 = I_3^{\max} sinc^2\left(\frac{\Delta k L}{2}\right)\,, \tag{3-4}$$

where $I_3^{\max}$ is the maximum intensity and L is the crystal length.

The reverse process, a pump wave producing two others with lower frequencies (down-conversion), could not occur, only if the desired wavelengths were also pumped. In this case, the method is parametric, because the crystal's proprieties are maintained, but not spontaneous, due to the necessity of the two frequencies in the input.

3.2 Spontaneous Parametric Down-Conversion

Now we shall analyze this case using the quantum mechanics formulation. To initiate is necessary to obtain the Hamiltonian of the system. Assuming the propagation of the wave along the z-axis, the operator electric field can be written as:

$$\hat{E}(z,t) = \hat{E}^{(+)}(z,t) + \hat{E}^{(-)}(z,t)\,, \tag{3-5}$$

with $\hat{E}^{(-)}(z,t) = \left[\hat{E}^{(+)}(z,t)\right]^{\dagger}$.

$$\hat{E}^{(+)}(z,t) = i\int_0^{\infty} A(\omega)\hat{a}(\omega)e^{i(k(\omega)z-\omega t)}d\omega\,, \tag{3-6}$$

where $A(\omega)$ is the amplitude, and $\hat{a}$, the annihilation operator. Therefore, the Hamiltonian is the pump, idler, and signal's electric field integrated over the volume V of the crystal [62].

$$\hat{H} = \epsilon_0\chi^{(2)}\int_V \hat{E}_p\hat{E}_s\hat{E}_i dV\,, \tag{3-7}$$

where ϵ_0 is the vacuum electrical permittivity and $\chi^{(2)}$ is the second-order susceptibility of the crystal.

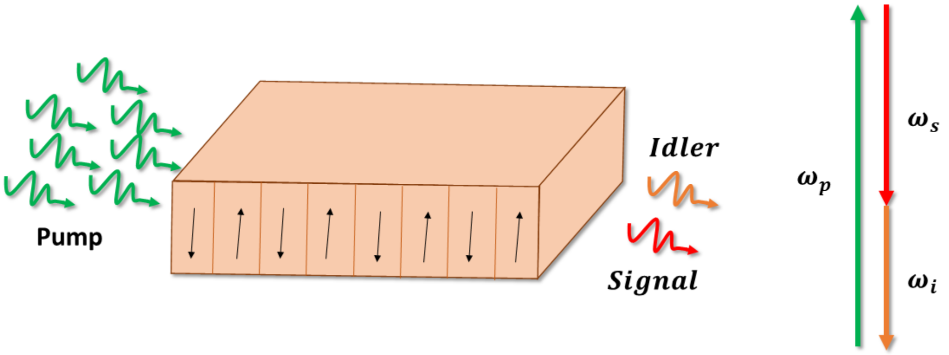

Figure 3.2: Illustration of Spontaneous Parametric Down-Conversion and the energy conservation of the process. ω_p, ω_s and ω_i refer to pump, signal and idler's frequenters, respectively.

Since no idler nor signal photon is entering the crystal, the initial state is the tensor product of their vacuum states, as equation 3-8 shows. This formalism, afforded by quantum mechanics, provides us to understand the process's spontaneity.

$$|\psi(0)\rangle = |0\rangle_s \otimes |0\rangle_i = |0,0\rangle = |0\rangle \tag{3-8}$$

The evolution of the system is:

$$|\psi(t)\rangle = U(t)\,|\psi(0)\rangle = e^{-i/\hbar\int_0^t dt' H(\hat{t'})}\,|0\rangle \tag{3-9}$$

Applying the Hamiltonian of the SPDC and the initial state into the equation 2-4, and using the first-order element of the Dyson series as an approximation [63, 64], the system's state is obtained.

$$\begin{aligned}|\psi(t)\rangle = (1+\chi^2)\,|0\rangle + \chi \int_0^t dt' \iiint_0^\infty d\omega_p d\omega_s d\omega_i \alpha(\omega_p)\times \\ \operatorname{sinc}(\Delta k L/2) e^{i\Delta k L/2} e^{i\Delta\omega t'} \hat{a}^\dagger(\omega_s)\hat{a}^\dagger(\omega_i)\,|0\rangle\end{aligned} \tag{3-10}$$

$\Delta\omega$ is the pump frequency minus signal and idler's frequency. $\alpha(\omega_p)$ is the pump spectrum. The amplitudes factors were pulled out as approximation, considering low variation with the frequency, so the parameter κ is:

$$\chi = i\frac{\pi L \epsilon_0 \chi^{(2)} A_p(\omega_p) A_s(\omega_s) A_i(\omega_i)}{\hbar} \tag{3-11}$$

The approximation in 3-10 is valid if the probability to generate a photon pair in the interaction time t is small. So it is used the limit $t \to \infty$, then the time integral becomes a Delta function of $\Delta\omega$. Hence, a simplified expression for the state is obtained:

$$\begin{aligned}|\psi\rangle =& (1+\chi^2)\,|0\rangle + \\ & \chi \iint_0^\infty d\omega_s d\omega_i N_\Psi \alpha(\omega_s+\omega_i) \operatorname{sinc}(\Delta k L/2) e^{i\Delta k L/2} \hat{a}^\dagger(\omega_s)\hat{a}^\dagger(\omega_i)\,|0\rangle\end{aligned} \tag{3-12}$$

By this equation, we shall obtain the essential element for the SPDC process study, the Joint-Spectral Amplitude (JSA). It is defined by the multiplication of the energy conservation, $\alpha(\omega_s + \omega_i)$ and phase-matching functions, $\Phi(\omega_s, \omega_i)$:

$$\Psi(\omega_s,\omega_i) = N_\Psi \alpha(\omega_s+\omega_i) \operatorname{sinc}(\Delta k L/2) e^{i\Delta k L/2} = N_\Psi \alpha(\omega_s+\omega_i) \Phi(\omega_s,\omega_i) \tag{3-13}$$

Where N_Ψ is such that $\iint d\omega_i d\omega_s |\Psi(\omega_s,\omega_i)|^2 = 1$. Using the JSA, one can consider the second order element of the Dyson series and obtain the following:

$$\begin{aligned}|\psi\rangle = (1+\chi^2)\,|0\rangle + \chi \iint_0^\infty d\omega_s d\omega_i \Psi(\omega_s,\omega_i)\hat{a}^\dagger(\omega_s)\hat{a}^\dagger(\omega_i)\,|0\rangle + \\ \frac{\chi^2}{2}\iint_0^\infty d\omega_s d\omega_i \Psi(\omega_s,\omega_i)\hat{a}^\dagger(\omega_s)\hat{a}^\dagger(\omega_i)\times \\ \iint_0^\infty d\omega_s' d\omega_i' \Psi(\omega_s',\omega_i')\hat{a}^\dagger(\omega_s')\hat{a}^\dagger(\omega_i')\,|0\rangle\end{aligned} \tag{3-14}$$

From this, we know that the probability of generating a pair is proportional to $|\chi|^2$, but also, the probability of generating two pairs is proportional to $|\chi|^4$, and no pairs, to $|1+\chi^2|^2$. Therefore, we conclude that the probability of generating no pairs is the greatest. Furthermore, since χ is proportional to the electrical field amplitude, one can easily conclude that SPDC is not an efficient process. Hence, we shall look for some figures of merit for the SPDC, which are, commonly, used to characterize these types o sources.

3.3
Purity and Single Value Decomposition

The first figure of merit is purity. From 0 to 1, this parameter weights how pure a state is. For the SPDC-based EPPS, we are interested in the spectral purity of the photons, which means that if the joint spectrum amplitude is not separable, the photons are pure. Moreover, If the source produces entangled photon pairs in a well-defined state, thus it is pure. Otherwise, they are mixed. Therefore, this parameter also evaluates the entanglement of the produced photons.

In this case, the purity of the entangled photon source is directly related to the shape of the Joint Spectral Amplitude, which is associated with the crystal material, crystal length, polling period, temperature, and pulse width. The following figure shows different shapes of Joint spectral intensity (JSI), the absolute square of the JSA [65].

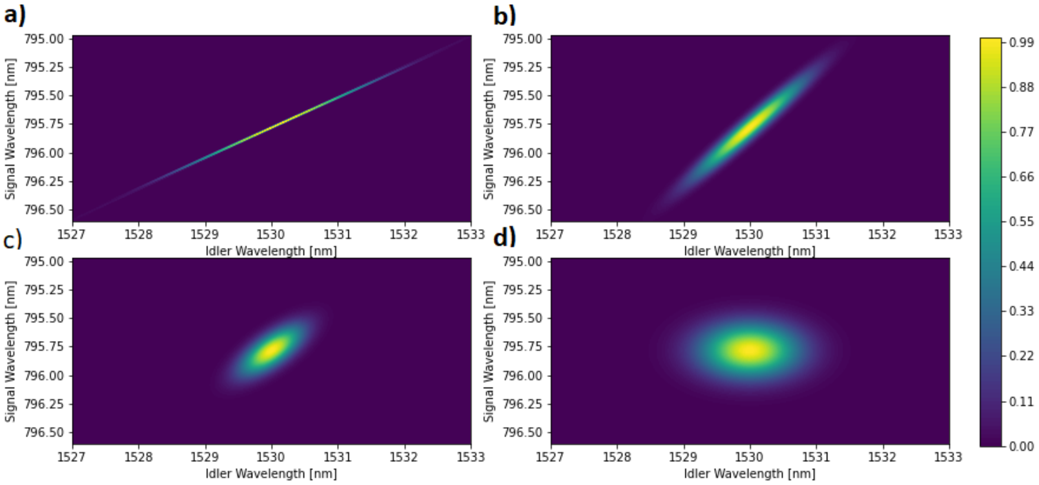

Figure 3.3: Different shapes for Joint Spectral Intensity, that leads to different purities. From a to d, the purity is gradually increasing, since the shape is getting more rounded. The purity for JSA a is $P_a = 0.02$; for JSA b, $P = 0.2$; for JSA c, $P_c = 0.7$; and for JSA d, $P_d = 1$.

To calculate the purity of the Joint-spectral amplitude, first, we have to decompose the Joint-Spectral amplitude into a basis of Hermitian functions using the Schmidt Decomposition. The expression 3-15 shows the decomposition of the JSA in terms of two orthonormal sets of Hermitian functions, $u_k(\omega_s)$ and $v_k(\omega_i)$. The r_k are the coefficients that weight this functions [66].

$$\chi\Psi(\omega_s, \omega_i) = \sum_k r_k u_k(\omega_s) v_k(\omega_i) \tag{3-15}$$

However, due to computational limits, we cannot use infinite number of coefficients and functions to decompose the JSA. Therefore, to apply this on the simulations, there is finite decomposition for matrices that approximates to the Schmidt Decomposition, The Singular Value Decomposition (SVD). In summary, the SVD is eigendecomposition, i.e., decomposes a square matrix in terms of its eigenvalues and eigenvectors. The expression 3-16 shows the decomposition of the $N \times N$ sampled JSA matrix in two matrix U and V, which are the eigenvectors matrices and R, a diagonal matrix with the eigenvalues in a descending order.

$$\chi\Psi_{N\times N} = U_{N\times N} R_{N\times N} V^T_{N\times N} \tag{3-16}$$

One can open this equation to see the similarities to the Schmidt decomposition in equation 3-15. The

$$\chi\Psi_{N\times N} = \begin{bmatrix} | & | & | \\ u_1 & \dots & u_N \\ | & | & | \end{bmatrix}_{N\times N} \begin{bmatrix} r_1 & 0 & 0 \\ 0 & \ddots & 0 \\ 0 & 0 & r_N \end{bmatrix}_{N\times N} \begin{bmatrix} - & v_1 & - \\ - & \vdots & - \\ - & v_N & - \end{bmatrix}_{N\times N} \tag{3-17}$$

We can simplify this into equation 3-18, which approximates to the Schmidt decomposition as N goes to infinity. Then, N has to be large enough to fulfill this approximation, but not too large so the computer can solve in a reasonable amount of time. In this work, we opted to use $N = 1000$, which compared with higher values of N, had the same results and it takes just some minutes to run. Figure 3.4 shows an example of modes and coefficients obtained from a SVD used in the simulations.

$$\chi\Psi(\omega_s, \omega_i)_{N\times N} = \sum_k^N r_k u_k(\omega_s) v_k(\omega_i) \tag{3-18}$$

From the coefficients of the decomposition, one can obtain the normalized ones, λ_k.

$$\lambda_k = \frac{r_k}{\sqrt{\sum_k r_k^2}} = \frac{r_k}{B} \tag{3-19}$$

Where B is called optical gain and it is the norm of r_k. Since $u_k(\omega_s)$ and $v_k(\omega_i)$ are orthonormal, it is trivial to notice that B^2 equals $|\chi|^2$. Then, using the normalized coefficients, one can calculate the purity of the generated states using:

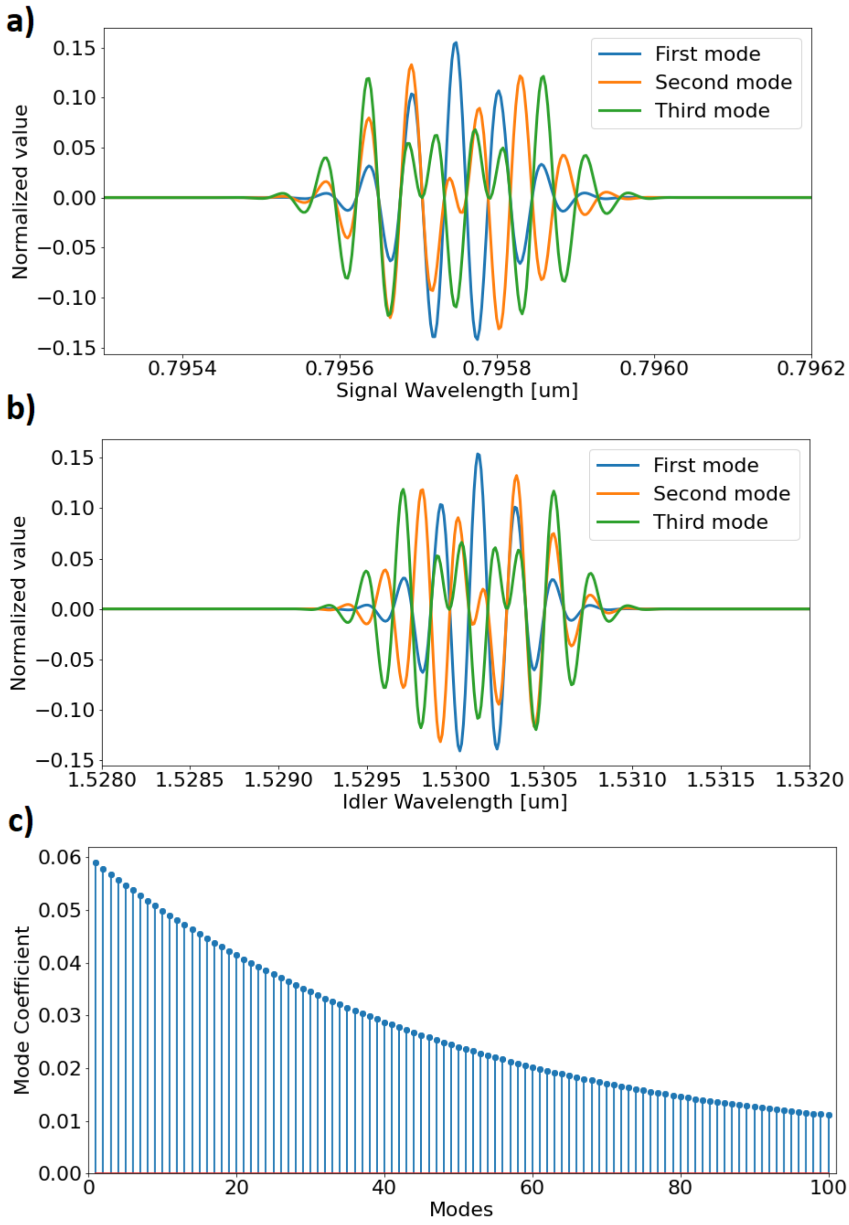

Figure 3.4: a) and b) Show the three most effective modes obtained form the SVD using $N = 1000$ for signal and idler, i.e, $u_k(\omega_s)$ and $v_k(\omega_i)$ for $k = 1, 2, 3$, respectively. c) Presents the first 100 coefficients obtained for this decomposition. This SVD uses the Joint-Spectral Amplitude developed in section 4.1.

$$P = \sum_k \lambda_k^4 \tag{3-20}$$

From the decomposition, we can define operators, which form a basis for the generated states.

$$\hat{A}_k = \int d\omega_s u_k(\omega_s)\hat{a}(\omega_s) \text{ and } \hat{B}_k = \int d\omega_i v_k(\omega_i)\hat{a}(\omega_i). \tag{3-21}$$

3.4
Second-Order Auto- and Cross-Correlation

Other important figures of merit are the second-order autocorrelation and cross-correlation functions, commonly called g2-auto and g2-cross, respectively. The g-auto estimates how close to a pure single photon the source is developing on idler and signal. The g2-cross evaluates the correlation between the two produced states. The great this value, the closer the generated state is to a maximum entangled state.

The correlation of nth-order is defined as a time-dependent function of the electromagnetic field. For quantized electric fields operators, we have [57]:

$$g^{(n)}(t_1,\ldots,t_n) = \frac{\langle \hat{E}^{(-)}(t_1)\ldots\hat{E}^{(-)}(t_n)\hat{E}^{(+)}(t_1)\ldots\hat{E}^{(+)}(t_n)\rangle}{\langle \hat{E}^{(-)}(t_1)\hat{E}^{(+)}(t_1)\rangle\ldots\langle \hat{E}^{(-)}(t_n)\hat{E}^{(+)}(t_n)\rangle} \tag{3-22}$$

Considering the jitter and efficiency of the detector, we shall introduce the detection time window, T(t), to the correlation [67].

$$g^{(n)} = \frac{\int dt_1 T(t1)\cdots\int dt_n T(t_n)\,\langle \hat{E}^{(-)}(t_1)\ldots\hat{E}^{(-)}(t_n)\hat{E}^{(+)}(t_1)\ldots\hat{E}^{(+)}(t_n)\rangle}{\int dt_1 T(t1)\,\langle \hat{E}^{(-)}(t_1)\hat{E}^{(+)}(t_1)\rangle\cdots\int dt_n T(t_n)\,\langle \hat{E}^{(-)}(t_n)\hat{E}^{(+)}(t_n)\rangle} \tag{3-23}$$

Then, considering that T(t) is constant for a short detection time, one can simplify the expression to:

$$g^{(n)} = \frac{\int^{(n)} dt_1\ldots dt_n\,\langle \hat{E}^{(-)}(t_1)\ldots\hat{E}^{(-)}(t_n)\hat{E}^{(+)}(t_1)\ldots\hat{E}^{(+)}(t_n)\rangle}{\int dt_1\,\langle \hat{E}^{(-)}(t_1)\hat{E}^{(+)}(t_1)\rangle\cdots\int dt_n\,\langle \hat{E}^{(-)}(t_n)\hat{E}^{(+)}(t_n)\rangle} \tag{3-24}$$

One can rewrite this expression using the annihilation and creation operators since the Electric field operator is proportional to the annihilation. Also, we can perform a Fourier Transform and operate on the frequency domain. Therefore, the resulting expression is:

$$g^{(n)} = \frac{\int^{(n)} d\omega_1\ldots d\omega_n\,\langle \hat{a}^\dagger(\omega_1)\ldots\hat{a}^\dagger(\omega_n)\hat{a}(\omega_1)\ldots\hat{a}(\omega_n)\rangle}{\int d\omega_1\,\langle \hat{a}^\dagger(\omega_1)\hat{a}(\omega_1)\rangle\cdots\int d\omega_n\,\langle \hat{a}^\dagger(\omega_n)\hat{a}(\omega_n)\rangle} \tag{3-25}$$

One can change the basis to use the basis defined for the generated states, and then [68]:

$$g^{(n)} = \frac{\langle : \left(\sum_k \hat{A_k}^\dagger \hat{A_k}\right)^n : \rangle}{\langle \sum_k \hat{A_k}^\dagger \hat{A_k}\rangle^n} \tag{3-26}$$

where $\langle : \cdots : \rangle$ is used to simplify the equation, indicating that the operators must be in normal order. Therefore, for the second-order autocorrelation, we obtain the following. [68].

$$g^{(2)} = 1 + \frac{\sum_k \sinh^4(r_k)}{\left(\sum_k \sinh^2(r_k)\right)^2} \tag{3-27}$$

For a low gain regime, i.e., for low values of r_k, one can use the approximation that $\sinh(r_k) \approx r_k$ and obtain the following:

$$g^{(2)} \approx 1 + \frac{\sum_k r_k^4}{\left(\sum_k r_k^2\right)^2} = 1 + \frac{\sum_k \lambda_k^4}{\left(\sum_k \lambda_k^2\right)^2} = 1 + \sum_k \lambda_k^4 = 1 + P \tag{3-28}$$

Therefore, for small values of B, the g2 is approximately 1 plus the purity.

Analogous, the nth-order cross-correlation depends on the quantized electric field. Hence, we consider the two systems to be Idler and Signal photons, i and s, respectively.

$$g^{(n,m)}(t_1^{(s)}, \ldots, t_n^{(s)}; t_1^{(i)}, \ldots, t_m^{(i)}) = \frac{\langle \hat{E}^{(-)}(t_1^{(s)}) \ldots \hat{E}^{(-)}(t_n^{(s)}) \hat{E}^{(+)}(t_1^{(s)}) \ldots \hat{E}^{(+)}(t_n^{(s)}) \times \hat{E}^{(-)}(t_1^{(i)}) \ldots \hat{E}^{(+)}(t_m^{(i)}) \rangle}{\langle \hat{E}^{(-)}(t_1^{(s)}) \hat{E}^{(+)}(t_1^{(s)}) \rangle \ldots \langle \hat{E}^{(-)}(t_n^{(s)}) \hat{E}^{(+)}(t_n^{(s)}) \rangle \times \ldots \langle \hat{E}^{(-)}(t_m^{(i)}) \hat{E}^{(+)}(t_n^{(i)}) \rangle} \tag{3-29}$$

Accomplishing the same step for the auto-correlation, one can get to [68]:

$$g^{(1,1)} = 1 + \frac{\sum_k \sinh^4(r_k)}{\left(\sum_k \sinh^2(r_k)\right)^2} + \frac{1}{\sum_k \sinh^2(r_k)} = g^{(2)} + \frac{1}{\sum_k \sinh^2(r_k)} \tag{3-30}$$

Considering a low gain regime, one can obtain:

$$g^{(1,1)} \approx 1 + P + \frac{1}{\sum_k r_k^2} = 1 + P + \frac{1}{B^2 \sum_k \lambda_k^2} \approx \frac{1}{B^2} \tag{3-31}$$

Since the optical gain is low, the term $1/B^2$ is greater than the other, thus it is dominant.

3.5 Visibility and Fidelity

From the calculation of the g2-cross, one can obtain another remarkable figure of merit for entangled photon sources, the visibility of entanglement. For better understanding, we shall consider the setup illustrated in figure 3.5-a, where we generate time-bin entangled photons. Each output goes to a Michelson interferometer, where there is a short and a long arm, l_1 and l_2, respectively. Therefore, idler and signal photons are time-bin encoded and entangled. If the photon goes through the short path, they are at the early state $|e\rangle$. Otherwise, they are at the late state, $|l\rangle$.

$$|\Phi^{+}\rangle = \frac{1}{\sqrt{2}}|ee\rangle + \frac{1}{\sqrt{2}}|ll\rangle \tag{3-32}$$

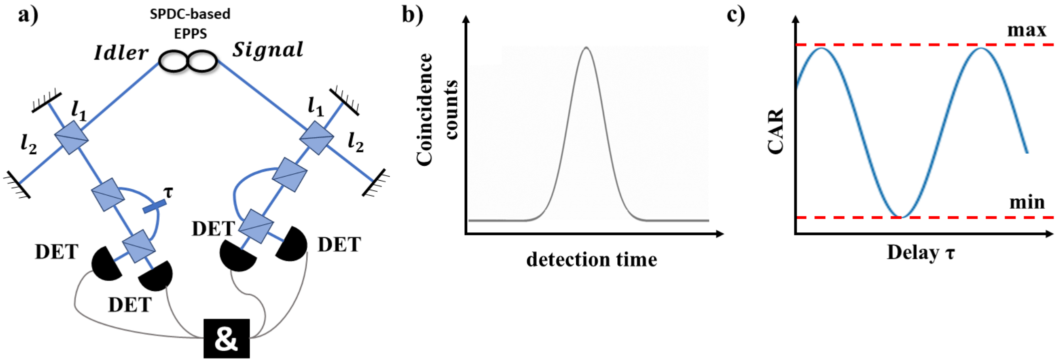

Figure 3.5: a) A simple setup for generating time-bin entangled photons and measuring the correlations. First, the entangled photons are generated by an SPDC source and the signal and idler photons are split into two arms. Both arms have a Michelson interferometer with a short and long path, l_1 and l_2, respectively. After this, the photons impinge a beam splitter, dividing into two arms, and both meet again on another BS, going to two photodetectors (DET). On one of the arms, there is a phase modulator that introduces a delay τ. Thus, the detection signals go to &, which counts the coincident counts. b) Shows the common interference pattern obtained in this experiment. c) Shows the coincidence-to-accidental ratio (CAR) for different values of τ.

After the generation of the states, they go through a beam splitter, which separates into two arms. On one of them, there is a phase modulator adding a delay τ. Then the arms meet again on another beam splitter, where the outputs are connected to photodetectors. The trigger signals of the detectors go to a system that counts the coincidences. Thus, figure 3.5-b illustrates an expected interference pattern obtained by this measurement. Varying τ and measuring the coincidence-to-accidental ratio for each of the curves obtained, one can get the result illustrated in figure 3.5-c. From this, one can calculate the visibility of entanglement using the following:

$$V = \frac{max - min}{max + min} \tag{3-33}$$

Note that this value belongs to the interval [0,1], where 1 means the photons are in a maximum entangled state and zero, thermal distribution. Besides, the states are entangled, only if, the visibility is higher than 1/3, and it violates the CHSH if it is higher than $1/\sqrt{2}$ [69, 70].

Since the visibility comes from the CAR, one can calculate it using the second-order cross-correlation by the following expression:

$$V = \frac{g^{(1,1)} - 1}{g^{(1,1)} + 1} \tag{3-34}$$

From the visibility, one can obtain another noteworthy figure of merit that measures how accurate the produced state is from a maximum entangled bell state, the fidelity. Before calculating this parameter, we shall simplify considering that our generated photon pair is an imperfect entangled state called the Werner state [71, 17]. Considering the setup illustrated in figure 3.5 and its outcome (eq. 3-32), one can represent the Werner state obtained by the following density matrix:

$$\rho^{\mathrm{EPPR}} = W \left|\Phi^{+}\right\rangle \left\langle\Phi^{+}\right| + \frac{1-W}{4} I_4 \tag{3-35}$$

Where I_4 represents the identity matrix of dimension 4×4 and W is the Werner parameter, which is the visibility of entanglement ($W = V$). Thus, the fidelity concerning the state $|\Psi^{+}\rangle$ by definition is:

$$F = \left\langle\Psi^{+}\right| \rho^{\mathrm{EPPR}} \left|\Psi^{+}\right\rangle \tag{3-36}$$

Therefore, one can write the Fidelity as a function of the visibility of entanglement.

$$F = \frac{3V + 1}{4} \tag{3-37}$$

3.6 Quantum Bit Error Rate and Secret Key Rate

Considering an entangled-based QKD protocol, two figures of merit are essential: Quantum Bit Error Rate and secret key rate. As we have seen in chapter 1, the most common sources for this yet are the EPPS based on SPDC. The performance of the generation of the entangled photons is the most influential on these parameters.

The QBER is, roughly, the ratio of the wrong qubits and all the qubits after sifting. During the QKD protocol, the two parties randomly choose qubits and sacrifice them to evaluate the QBER. As a security measure, they know that the key is secret if the QBER is lower than 11% [40]. However, to understand the reasons for these mistaken qubits and to estimate them, it is fundamental to unravel the QBER. Therefore, one can write open the QBER into three components [72].

$$Q = Q_{\mathrm{det}} + Q_{\mathrm{acc}} + Q_{\mathrm{opt}} \tag{3-38}$$

The first component, Q_{det}, agglomerates the errors due to the efficiency and dark counts of the detectors and the distance. The second term, Q_{acc}, considers the accidental counts due to multiphoton emission, i.e., the source generates more than one pair simultaneously. For SPDC-based sources, this parameter is related to the pump intensity. As we can see in equation 3-14, the probability amplitude of producing two pairs goes with the square of χ, which is proportional to the square root of the pump intensity.

The last component, Q_{opt}, depends only on the performance of the source to generate entangled states. Therefore, one can calculate this element using the visibility of the interference pattern of the entangled photons pairs emitted [72].

$$Q_{\text{opt}} = \frac{1-V}{2} \tag{3-39}$$

For future calculations, we shall consider the other terms than Q_{opt} negligible for the QBER. From the QBER, we can calculate the ratio of keys generated and qubits received, or the Shor-Preskill bound, using the following expression [56].

$$E = 1 - (\kappa + 1)H(Q) \tag{3-40}$$

Where $H(\cdot)$ is the Shannon Entropy [73]:

$$H(Q) = -Q\log_2(Q) - (1-Q)\log_2(1-Q) \tag{3-41}$$

And κ is the reconciliation efficiency, which, for perfect reconciliation, is 1. As the efficiency degrades κ increases. Using equation 3-40, one can obtain the cutoff QBER (Q_c), i.e., the highest error rate, for which the ratio is positive. Table 3.1 presents some examples of the reconciliation efficiencies and their respective cutoff QBER. Besides, that is the reason qubits with QBER higher than 11% cannot be used as keys.

κ	1	1.11	1.22
Q_c	0.11	0.101	0.094

Table 3.1: Table for different reconciliation efficiencies (κ) and their Quantum Bit Error Rate cut off Q_c.

With these values in hand, we can estimate the secret key rate (SKR):

$$SKR = R \times P_{A-B} \times E \tag{3-42}$$

Where R is the pump pulse rate, P_{A-B} is the probability of a pair reaching A and B (final nodes), and E is the rate of secret keys per pair received. The pulse rate is commonly tunable. Therefore, only the probability remains unknown. This parameter will depend on the chosen setup, for example, the ones shown in chapter 1 for the quantum relay and quantum repeater. In the next chapter, we shall simulate and analyze the usage of the SPDC-based source for frequency multiplexed BBM92.

4
Simulations and Analysis

In this chapter, we shall apply the knowledge we have gathered to simulate an SPDC-based entangled photon pair source. The objective of this work is to investigate the source characteristics and related parameters for a frequency multiplexed quantum repeater setup. More specifically, we consider a QR similar to the one presented in [27].

Therefore, we engineered the crystal and the pump so that the resulting idler and signal are about 1550 and 795 nm, respectively. The idler wavelength matches with the Erbium-based quantum memory, and, on the other hand, the idler matches with Thulium-based QM. Besides, the C-band, which contains the idler's wavelength, has the lowest loss on optical fibers.

First, we shall understand how to make the simple simulation of the SPDC. Understand the functions that constitute the Joint-Spectral Amplitude and which parameters are relevant to this phenomenon. Then, we can change these parameters and see the effects on the figures of merit. See the performance of the SPDC as a source for a direct transmission of keys on a BBM92 protocol.

Finally, we shall apply filters on the JSA and multiplex signal and idler into frequency channels. Subsequently, use this frequency multiplexed SPDC as a source for a BBM92 and compare the results to the direct transmission. Besides, analyze and compare different configurations.

4.1
Joint-Spectral Amplitude and Intensity

The nonlinear crystal and pump must fulfill the energy conservation and quasi-phase-matching conditions to achieve the desired bands, B and C. We shall use a periodic poling Lithium Niobate crystal (ppLN), in which the highest element of the second-order susceptibility tensor is $-20,6$ pm/V (propagation axis) [74] and 7 μm of periodic poling. During the simulations, we manage the pump laser wavelength of 523,5 nm and temperature of 40 degrees Celsius to obtain the idler wavelength of 1530 nm and signal of 795,7 nm.

To simulate the JSA, equation 3-13, we have to split it into two functions: the energy conservation, alpha, and the phase matching, Phi. The energy conservation function corresponds to the normalized spectrum of the pump. Considering Gaussian pulses for the pump, one can write alpha as:

$$\alpha(\omega_s+\omega_i) = e^{-2\pi^2\sigma_t^2[\omega_p-(\omega_s+\omega_i)]^2} \tag{4-1}$$

Where σ_t is related to the pulse width, Δt, full width at half maximum (FWHM):

$$\sigma_t = \frac{\Delta t}{2\sqrt{\ln 2}} \tag{4-2}$$

Considering a pulse width of 50 ps the energy conservation function obtained is in figure 4.1.

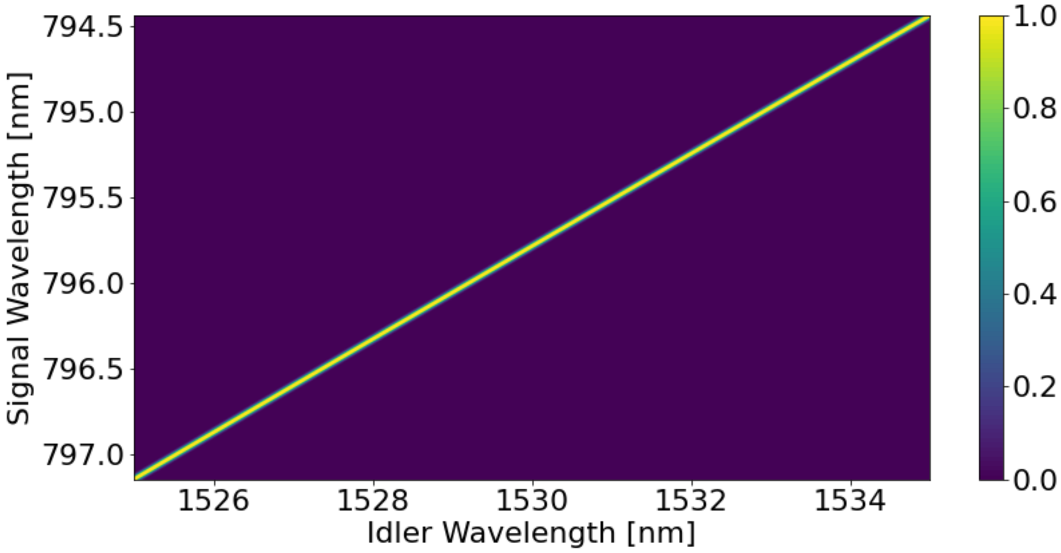

Figure 4.1: Energy conservation function for Gaussian pulse with 50 ps of FWHM.

In equation 3-13, find the definition for the phase-matching function. This function depends on the quasi-phase-matching parameter Δk, which is in equation 3-3. Expanding this equation, one obtains the following:

$$\Delta k = 2\pi\left(\frac{n_p}{\lambda_p} - \frac{n_p}{\lambda_p} - \frac{n_p}{\lambda_p} - \frac{1}{\Lambda}\right) \tag{4-3}$$

In order to evaluate the refractive index inside the crystal for each wavelength, we use a temperature-dependent Sellmeier equation as suggested in [75]. The Sellmeier equation used in the simulation is presented in 4-4, where n_e is the refractive index. The parameters a_1 to a_6 and b_1 to b_4 are constants empirically obtained and f is calculated by an temperature-dependent equation.

$$n_e^2 = a_1 + b_1 f + \frac{a_2 + b_2 f}{\lambda^2 - (a_3 + b_3 f)^2}\frac{a_4 + b_4 f}{\lambda^2 - a_5^2} - a_6\lambda^2 \tag{4-4}$$

After the polling period is set, it is adjusted considering the thermal expansion, as proposed in [76]. The equation 4-5 demonstrates how it was implemented in the simulation. In 4-5, Λ is the polling period after the expansion, Λ_0 is the pre-determined one, T_0 is 298.15 K, the coefficients α_0 and α_1 are constants empirically obtained.

$$\Lambda(T) \approx \Lambda_0 + [\alpha_0(T - T_0) + \alpha_1(T - T_0)^2] \tag{4-5}$$

After calculating the refractive index inside the crystal and the polling period for the simulation temperature, we can calculate the phase-matching function. Considering a 10 mm crystal, $\Lambda = 7\ \mu$m and a temperature of 40° C.

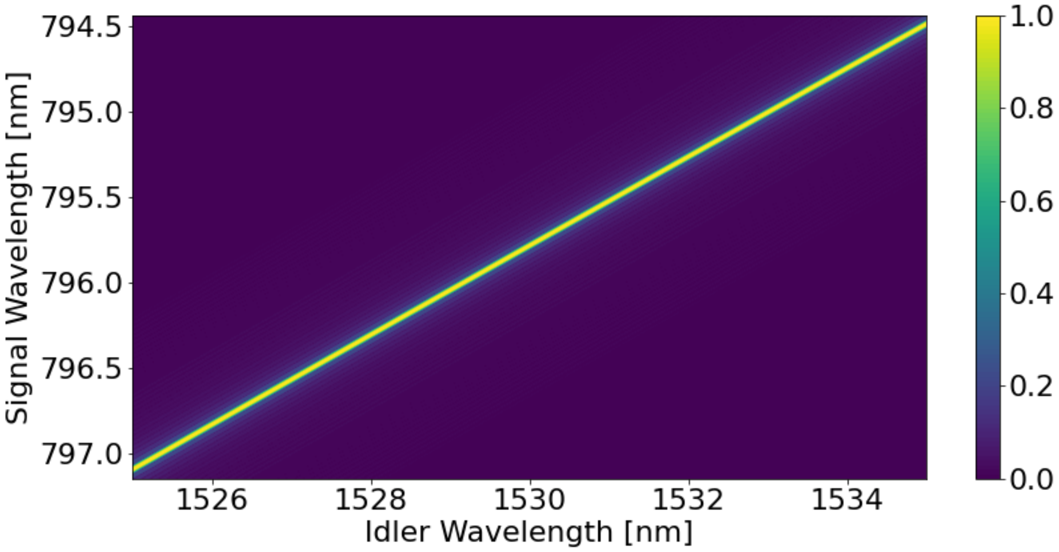

Figure 4.2: The absolute of the phase-matching function for a 10 mm crystal, with polling period of $\Lambda = 7\ \mu$m and at 40° C.

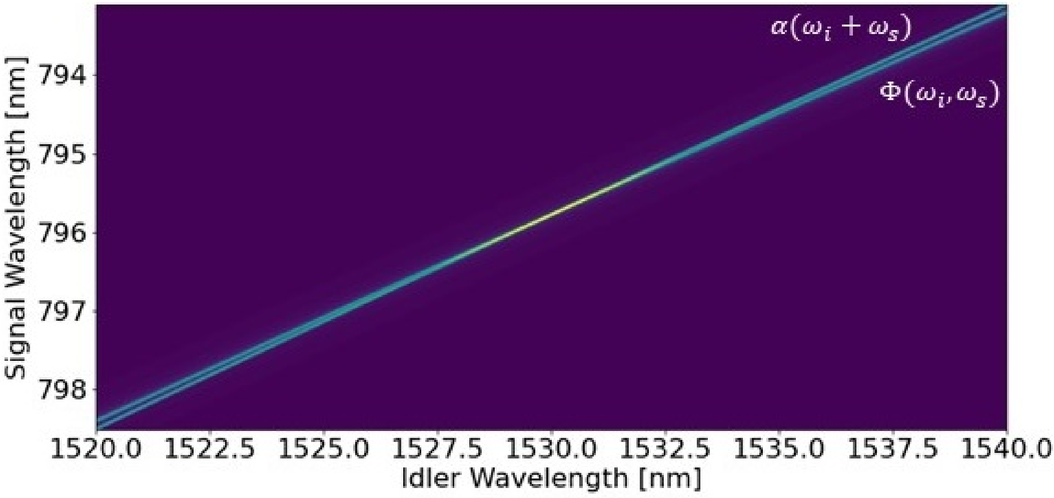

Figure 4.3: The overlapping region between the function of figure 4.1 and 4.2.

Then, the JSA is the overlapping region between these two functions, $\alpha(\omega_i + \omega_s)$ and $\Phi(\omega_i, \omega_s)$, as the figure 4.3. Therefore, the resulting Joint Spectral Intensity is illustrated in figure 4.4. We use the intensity because the JSA function is complex.

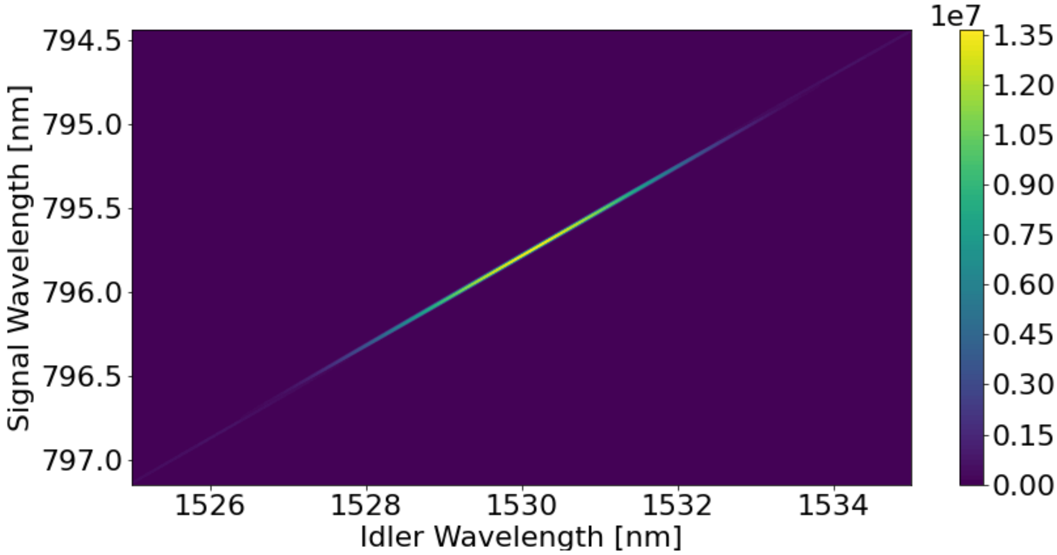

Figure 4.4: Joint-Spectral Intensity using the specification of figure 4.1 and 4.2.

Before continuing, it is essential to understand the effect of some parameters on the JSA shape. The energy conservation function width is inverse proportional to the pulse width. The phase-matching function and crystal length have a similar relation. After choosing the crystal type, the temperature controls idler and signal wavelengths because it changes the phase-matching function slope [65].

4.2 Figures of Merit and Key distribution

Assuming that the pump power is adjusted to result in a mean number of pairs per pulse of 0.1 ($\mu = |\chi|^2 = 0.1$), one can calculate the figures of merit for the source described in the previous section. First, we shall use the singular value decomposition, equation 3-18, to obtain the coefficients, then we calculate the purity and the second-order cross-correlation. Using the single value decomposition, using equations 3-20 and 3-30, respectively.

$$P = 0.016 \text{ and } g^{(1,1)} = 11.02 \tag{4-6}$$

The parameters of the pump laser and the crystal produce energy conservation and phase-matching function with close slopes, as figure 4.3 shows. Therefore, the JSI, figure 4.4, has this stretched shape, which causes this low purity.

Note, in this case, $g^{(1,1)}$ is approximately $1+P+1/B^2$, which is following equation 3-31. One can calculate the visibility using this value and equation 3-34. And, following the steps of the previous chapter, we can also obtain the estimation of the QBER and the key rate per photon arriving considering a reconciliation efficiency of $\kappa = 1.1$.

$$V = 0.8336 \tag{4-7}$$

$$Q = 0.0831 \tag{4-8}$$

$$E = 0.132 \tag{4-9}$$

Now, with these figures of merit, we can use this source to transmit qubits directly. Then, calculate the achievable secret key rate for this source using equation 3-42. However, we first have to define the probability (P_{ab}) of the photons arriving at the receivers. Since we are considering direct transmission, P_{ab} is the probability of generating pairs, $p(n > 0)$, times the probability of it arriving at the other side and origin a detection on both sides. For simplicity, we consider the source close to A, so the attenuation for the signal photon is negligible. Then, the idler photons go through an optical fiber of length d.

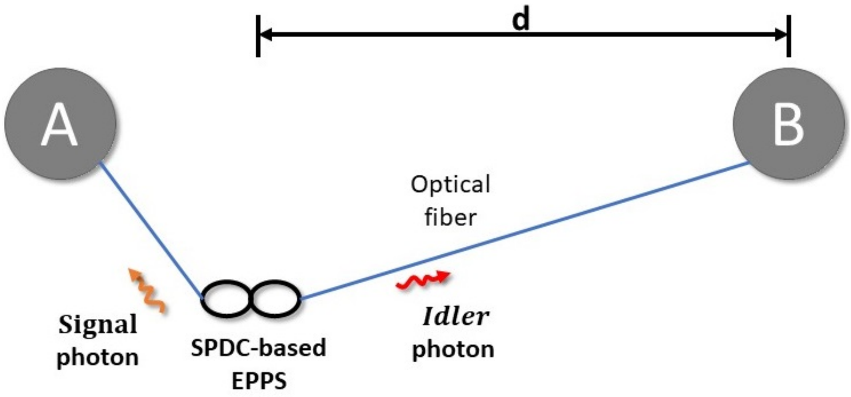

Figure 4.5: Scheme for the simulation of direct transmission. We consider that A is so close to the source that the distance is negligible.

Therefore, the probability of A and B receiving a pair is:

$$P_{ab} = \eta_{det}^2 e^{-\alpha d} p(n > 0) \tag{4-10}$$

To calculate the likelihood of the source emitting pairs, we shall remember the distribution of the SPDC process, equation 3-14. However, since we are looking only for the probabilities, we can simplify and look only for the coefficients of the Dyson series [63]:

$$|\psi_{SPDC}\rangle = (1+\chi^2)\,|0,0\rangle + \sum_{n=1}^{\infty} \frac{\chi^n}{n!}\,|n,n\rangle \tag{4-11}$$

Then, the probability of having one or more pairs from the source is the projection on all the $|n, n\rangle$, where $n \in \mathbb{N}^*$. Therefore, one can write the following:

$$p(n > 0) = \sum_{n'=1}^{\infty} \frac{|\langle n', n'|\psi_{SPDC}\rangle|^2}{|\langle \psi_{SPDC}|\psi_{SPDC}\rangle|^2} = \frac{\sum_{n=1}^{\infty} \frac{|\chi|^{2n}}{(n!)^2}}{|\langle \psi_{SPDC}|\psi_{SPDC}\rangle|^2} \tag{4-12}$$

The norm of $|psi_{SPDC}\rangle$ is:

$$|\langle \psi_{SPDC}|\psi_{SPDC}\rangle|^2 = |1+\chi^2|^2 + \sum_{n=1}^{\infty} \frac{\chi^{2n}}{(n!)^2} = |1+\chi^2|^2 + I_0(2|\chi|) - 1 \tag{4-13}$$

Where $I_0(x)$ is the modified Bessel function of the first kind [77]. Therefore, one can rewrite equation 4-12 using this and the $\chi^2 = -\mu$ and $\chi^2 = -\mu$ (eq.3-11):

$$p(n > 0) = \frac{I_0(2\sqrt{\mu}) - 1}{|1-\mu|^2 + I_0(2\sqrt{\mu}) - 1} \tag{4-14}$$

We can calculate the achievable secure key rate for different distances by adjusting the pump pulse rate to 100 MHz and assuming the attenuation of fiber 0.2 dB/km.

$$SKR_{\text{dir}} = R\,E\,Pab \tag{4-15}$$

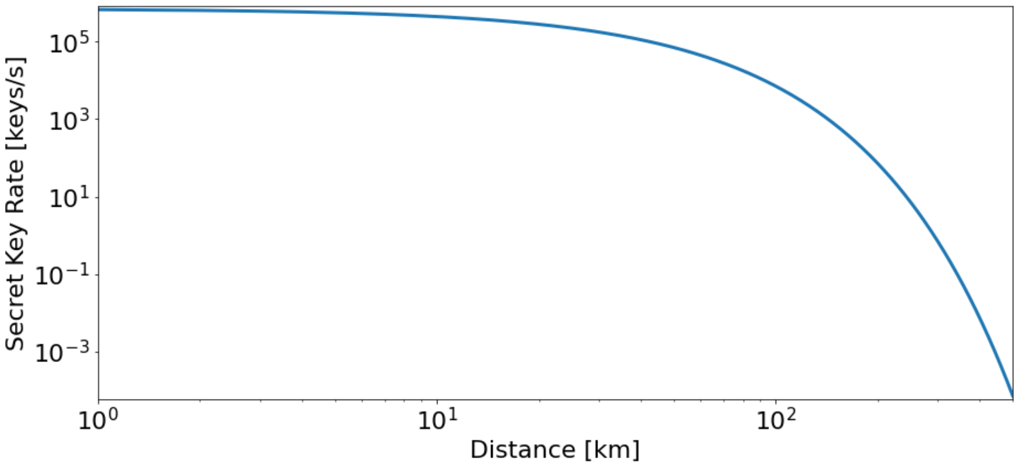

Figure 4.6: Achievable secret key rate using the SPDC-based source developed in the previous section with a pump rate of 100 MHz.

4.3 Filtering Signal and Idler

One can implement a frequency multiplexed quantum repeater protocol to reach further distances without compromising the secret key rate [24]. As we have seen in the first chapter, multiple modes increase the chance of successful entanglement distribution.

To multiplex the photon pairs, one must generate them in close bands and split each channel. One typical way of doing so is using a cavity-enhanced SPDC, i.e., putting the nonlinear crystal used for SPDC inside a cavity structured for the signal and idler wavelengths [55]. Furthermore, one can implement the channel separation using a Virtually-Imaged Phased Array (VIPA) as a mapper [78].

To simulate this scenario, we opted to use an array of lossless filters matched to the signal and idler central wavelengths. Therefore, we can emulate the results of a cavity-SPDC and have more control of the number and bandwidth of channels. Hence, we calculate the filtered JSA using the following [79].

$$\Psi_{\text{filtered}}(\omega_i, \omega_s) = \Psi(\omega_i, \omega_s) A_i(\omega_i) A_s(\omega_s) \tag{4-16}$$

Here and after, when we use filter bandwidth, the reader shall consider this value for signal and idler filters. Both filters' bandwidths are matched in frequency to achieve the best purity. Moreover, the centers of the filters are matched following the energy conservation equation.

Using the JSA we have been developing, we can implement filters and analyze the impact on the source figures of merit. Figure 4.7 exhibits the previous JSA after filters with 10 GHz bandwidth. We increased the pump power until the filtered μ result was 0.1. to maintain consistency. Note the JSA shape got more rounded, which directly affected the purity, increasing it to 0.749. On the other hand, the second-order cross-correlation did not improve much since we managed to maintain the average number of photons and the g2cross is approximately inversely proportional to this (see equation 3-31).

To implement multiple filters, we shall first analyze the behavior of these figures of merit on different parts of the spectrum. Then, we can define the total bandwidth to split into multiple channels. Therefore, we sweep the central wavelength of the filters and evaluate for each case the average pair number, purity, and second-order cross-correlation.

We can define these different values of central wavelength as a possible channel. Accordingly, the figures give us the parameters for choosing the bandwidth best suits our scenario. Analyzing figure 4.8, we see that the purity

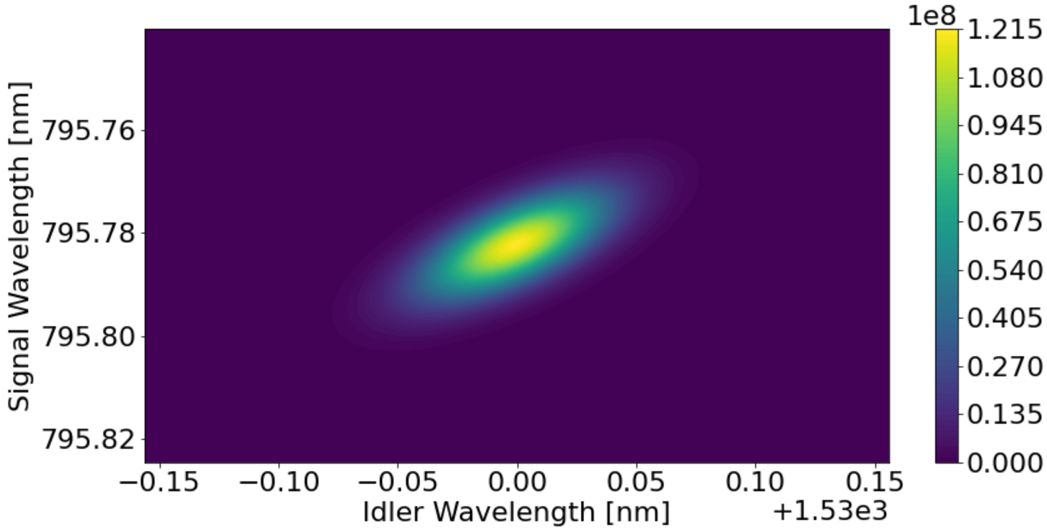

Figure 4.7: The filtered JSI using the previous conditions and filters bandwidth of 10 GHz. This JSI is multiplied by the χ^2. The pump power was adjusted so we obtain $\mu = 0.1$, i.e., integrating this function over the idler and signal wavelengths, we obtain 0.1.

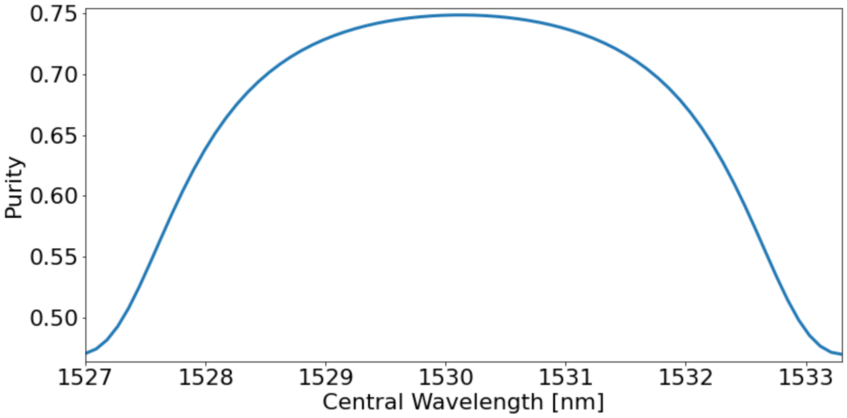

Figure 4.8: Purity sweeping the central wavelength of the filters, using a 10 GHz filter.

degrades as the filter departs from the center of the JSA. This effect is due to the peripheral filtered JSA shape being less rounded than the centered. In opposition to this effect, figure 4.9 shows the $g^{(1,1)}$ increasing as the filter departs from the center. To understand this, look for the behavior of the μ in figure 4.10. Remember that $g^{(1,1)}$ is approximately one over μ (eq. 3-31). Therefore, since the average photon number reduces, the second-order cross-correlation increases.

Looking only for the g2 values does not give us a clue about the operating bandwidth for the channels since it only increases. Therefore, using the average photon pair, one can determine the lowest μ they accept, then define a bandwidth for the channels. Here and after, we shall use the limiting μ as

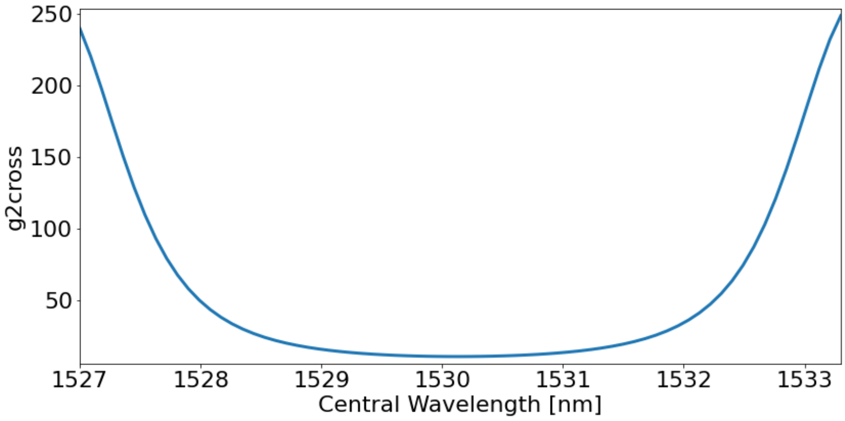

Figure 4.9: Second-order cross-correlation sweeping the central wavelength of the filters, using a 10 GHz filter.

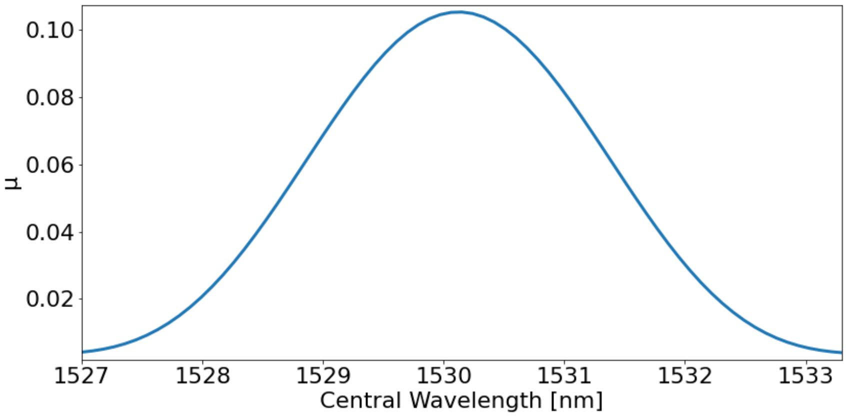

Figure 4.10: Average photon pair number sweeping the central wavelength of the filter, using a 10 GHz filter.

one-quarter of the maximum, in this case, 0.025. Using this specification, the operating band we got for this setup is approximately 530 GHz. Thus, we can define an equation for the maximum number of channels.

$$N_{\text{chan}} = \frac{B_{\text{op}}}{\alpha_{\text{occ}} B_{\text{filter}}} \tag{4-17}$$

N_{chan} represents the maximum number of channels, B_{op} is the operating band for the channels, B_{filter} is the filter bandwidth and α_{occ} is the occupation factor. The occupation factor is the ratio of channel and filter bandwidth. Considering $\alpha_{\text{occ}} = 2$, we obtain a maximum of 26 channels to use.

Moreover, another important step for the channels is defining the pump pulse rate since the filtering broads the pulses. We shall understand this problem more as we further into it. First, we must obtain the marginal spectrum for signal and idler. The equation for the marginals is as follows.

$$|\Psi_{\text{idler}}(\omega_i)|^2 = \int d\omega_s |\Psi(\omega_i, \omega_s)|^2 \tag{4-18}$$

$$|\Psi_{\text{signal}}(\omega_s)|^2 = \int d\omega_i |\Psi(\omega_i, \omega_s)|^2 \tag{4-19}$$

Therefore, using these equations, one can apply the filtered JSA (developed before) and obtain the marginals in figure 4.11.

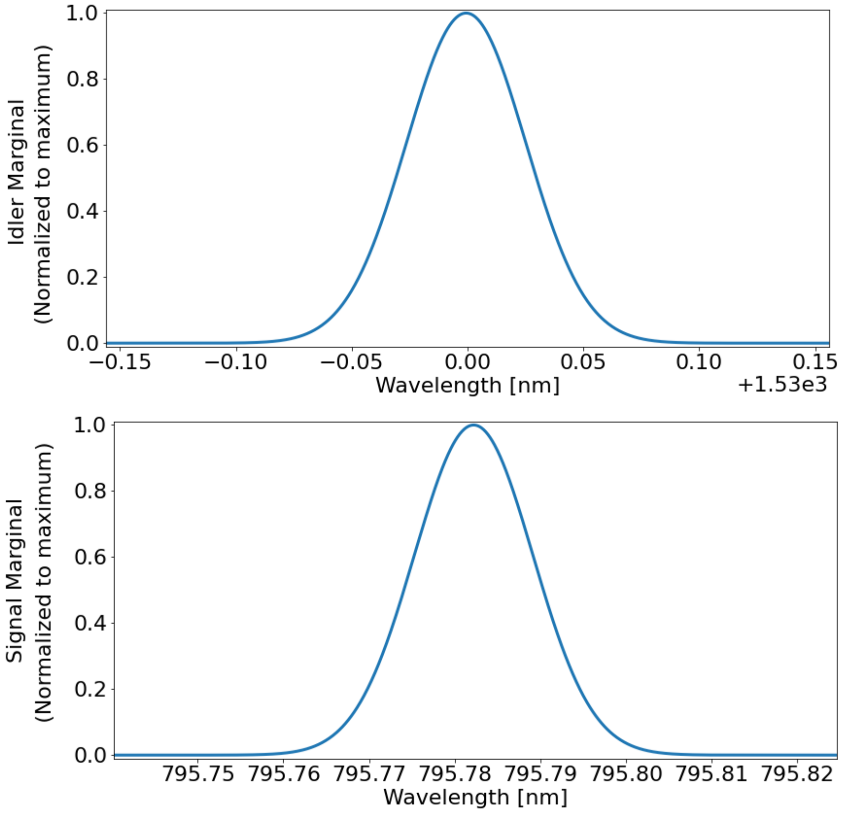

Figure 4.11: Marginals Spectrum for Signal and Idler after a 10 GHz filter.

Assuming the marginals are Gaussians, one can calculate the pulse in the time domain. Figure 4.12 presents the idler pulse for this marginal.

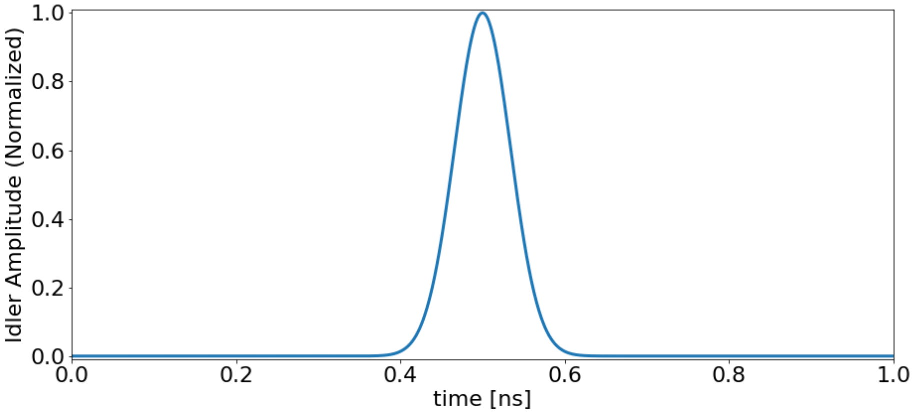

Figure 4.12: Idler pulse obtained from the marginals in figure 4.11.

Considering the repetitions of the pump pulse, we can replicate these pulses dislocated T from each other, where T is $1/R$. Figure 3 shows the pulses from figure 2 for two rates: 1 GHz and 10 GHz.

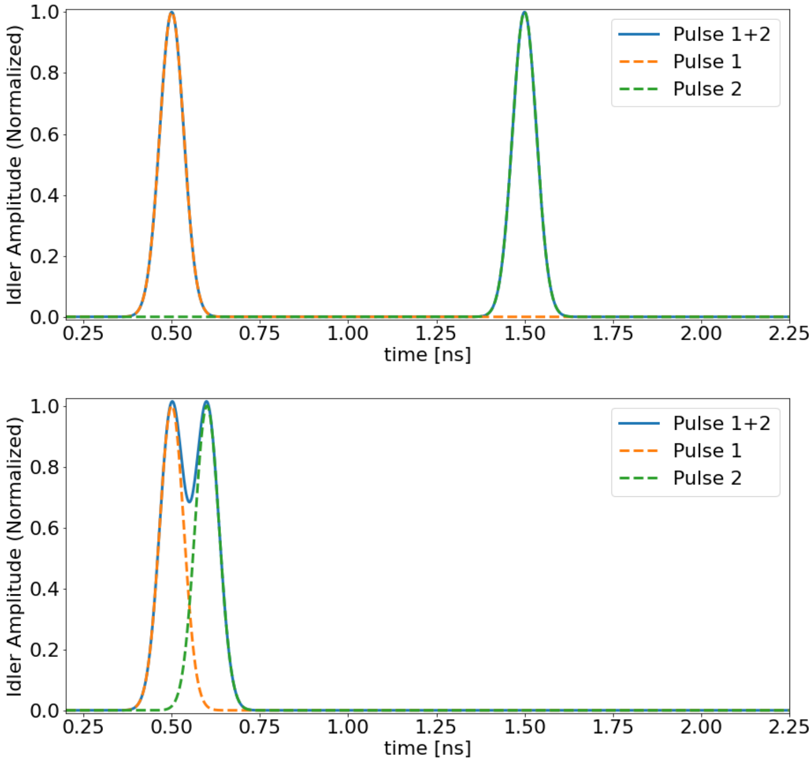

Figure 4.13: Two idler pulses generated by the source for different pump pulse rates. On top, the pump rate is 1 GHz, and the other is 10 GHz, which corresponds to the filter bandwidth.

We shall look forward to the crosstalk between the generated envelopes to analyze the effect of this overlapping. The crosstalk measures the influence of the neighboring pulses in a pulse time slot. Accordingly, one can define the crosstalk as follows.

$$C = \frac{\int_{(n'-1)T/2}^{(n'+1)T/2} |\sum_n p(t+nT)|^2 dt - \int_{(n'-1)T/2}^{(n'+1)T/2} |p(t+n'T)|^2 dt}{\int_{(n'-1)T/2}^{(n'+1)T/2} |p(t+n'T)|^2 dt} \qquad (4\text{-}20)$$

Where the function $p(t)$ represents the envelope of the pulse and the integral is throughout the n' pulse. Figure 4.14 shows the crosstalk for different pulse rates fixing the filter bandwidth at 10 GHz. From this, we can define limiting crosstalk to choose the best pump rate for the source. Therefore, choosing the maximum crosstalk of -60 dB, we get the maximum rate of approximately 3.8 GHz.

Considering this limit of -60 dB for the crosstalk, we can calculate the maximum rate for different filters' bandwidths using the simulations. In

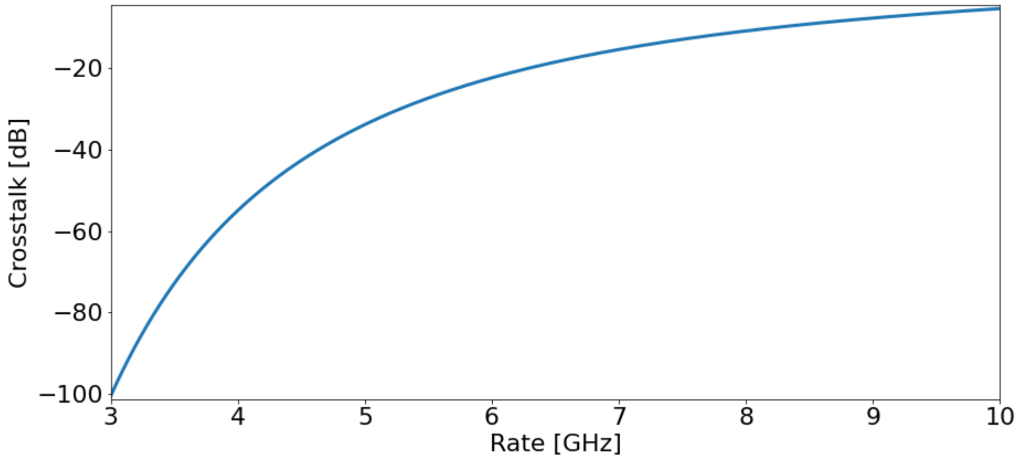

Figure 4.14: Corsstalk sweeping the pump rate for a 10 GHz filter.

addition, we can use equation 4-17 and the value obtained by the simulations for the operating band, i.e., 530 GHz, to calculate the achievable number of modes as a function of the filter's bandwidth. Thus, figure 4.15 shows the resulting curves for these calculations on the same plot. Moreover, the green dashed lines indicate the corresponding rate and number of modes for the 1GHz bandwidth filter chosen, which are 3.8 GHz and 26, respectively.

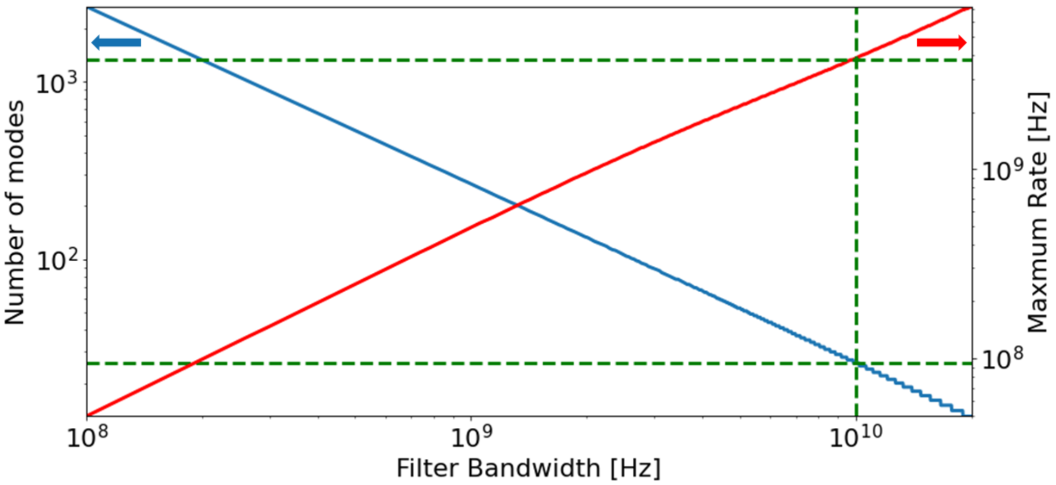

Figure 4.15: The achievable number of modes and the maximum rate considering the -60 dB crosstalk limit as functions of the filter bandwidth. The curve in blue corresponds to the number of modes. On the other hand, the red curve represents the maximum rate. Moreover, the values for the 10 GHz filter used in this work are highlighted by the green dashed lines, i.e., $R = 3.8$ GHz and 26 Channels.

4.4 Frequency Multiplexed Key Distribution

Now, we shall define the setup for multiple channels to implement the filtered SPDC source created in the last section. Based on figure 4.5, we can introduce mappers using the VIPA as in article [78], to split the channels at A and B. Figure 4.16 defines the scheme for this.

To analyze the system performance, one can look for the secret key rate described in equation 3. First, we shall define the expression for the probability of a pair reaching A and B, P_{ab}. Analogous to what we have done in chapter 1 for the quantum memories, we shall look for the scenario of getting no photons, then find the complement of this event.

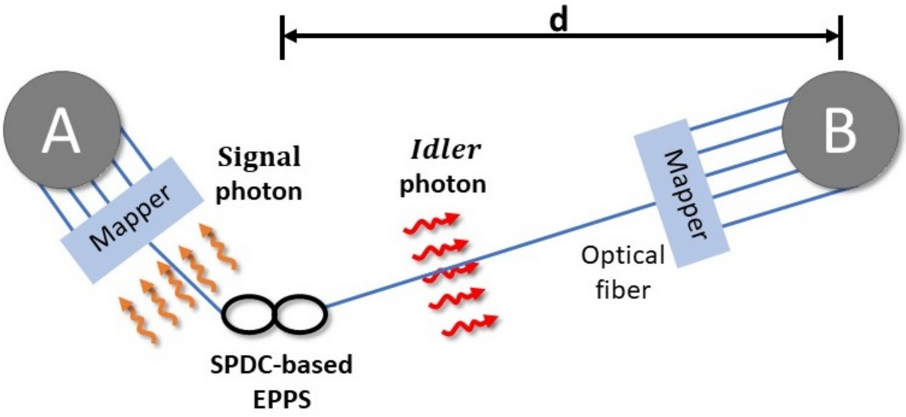

Figure 4.16: Setup for distributing entangled photons from multiple channels generated by the filtered SPDC source.

Therefore, the probability of no photons reaching A or B for a single channel is:

$$P_m = 1 - (\eta_{det}\eta_{map})^2 e^{-\alpha d} p_m(n > 0) \tag{4-21}$$

Where $p_m(n > 0)$ is the probability of the mth mode generating pairs, similar to equation 4-14, but for the mode m. Moreover, μ_m is the average number of photons per pulse.

$$p_m(n > 0) = \frac{I_0(2\sqrt{\mu_m}) - 1}{|1 - \mu_m|^2 + I_0(2\sqrt{\mu_m}) - 1} \tag{4-22}$$

Back to equation 4-21, η_{det} and η_{map} are the efficiencies of the detection and mapping, respectively. Although the VIPA used in [78] shows a dependency of the frequency on the efficiency, i.e., it degrades as the wavelength departs from the central, the operating bandwidth of the source is narrow enough to consider the efficiency constant. Since the channels are not correlated, the probability for all M channels together is the product of them. Accordingly, we can now define P_{ab}, which is the complement of this product.

$$P_{ab} = 1 - \prod_{m}^{M} \left[1 - (\eta_{det}\eta_{map})^2 e^{-\alpha d} p_m(n > 0)\right] \tag{4-23}$$

After defining P_{ab}, we shall calculate the secret key per qubit received. Since we cannot insert this parameter into a product of the probabilities, we consider the average key rate per qubit received weighted by the probability of only one mode being successful. Thus, first, we shall calculate this probability, $p(m)$.

$$p(m) = \left[\prod_{k=1,k\neq m}^{M} p_k(n = 0)\right] p_m(n > 0) \tag{4-24}$$

Where $p_m(n > 0)$ comes from equation 4-22 and $p_m(n = 0)$ is the complement to this.

$$p_m(n = 0) = 1 - p_m(n > 0) = \frac{(|1 - \mu_m|^2)}{(|1 - \mu_m|^2) + I_0(2\sqrt{\mu_m}) - 1} \tag{4-25}$$

Therefore, the weighted average secret key per qubit received, $[E]$, is given by the following:

$$[E] = \sum_{m=1}^{M} p(m) E_m \tag{4-26}$$

Where E_m is the Shor-Preskil bound, defined by eq. 3-40, but calculated for each mode m. It is relevant to stress the fact that this calculation is an approximation and gives the lower bound for the actual secret key per qubit rate. It is a lower bound because we are not considering that multiple modes can have success. Moreover, the multiple success implicates that the receiver must make a choice on which mode to use. Here, we can create a criterion for this. Looking at figure 4.9, one can conclude that the modes far from the center have better visibility. Therefore, the criterion is to choose the success mode that is further from the central mode.

Using equations 4-23 and 4-26, one can define the expression for the secrete key rate, SKR.

$$SKR = R\, P_{ab}\, [E] \tag{4-27}$$

Using equation 4-27, we can implement a simulation for this scenario at different distances. For this simulation, we must have some assumptions. First, the detector and mapper efficiencies are constants for all the modes and are 0.7 and 0.5, respectively. Accordingly to the last section, our criterion for the μ and filter allows us to use 26 channels, and the maximum pump rate is 3.8

GHz. Therefore, using these values, we obtain the graph illustrated in figure 4.17.

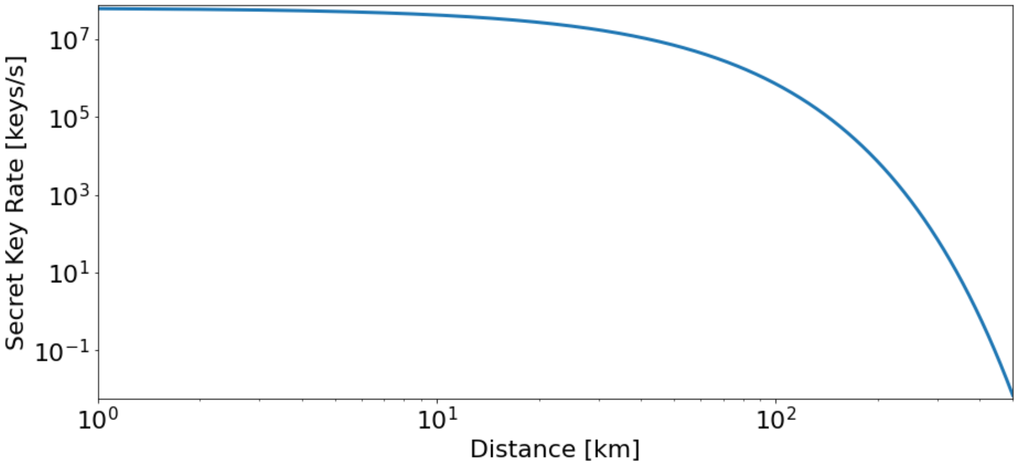

Figure 4.17: Secret key rate over the distance between A and B for 26 channels and pump rate of 3.8 GHz. Besides, the detector and mapper efficiencies were considered constant for every channel, 0.7 and 0.2, respectively. The fiber attenuation is 0.2 dB/km and also constant for all the modes.

Finally, we can analyze the SPDC source: the influence of the mean photon number on the secret key rate. μ is tunable by changing the intensity of the pump pulses since they are directly proportional. As it increases, the probability of photons reaching A and B increases. However, the QBER enhances because the second-order cross-correlation is, approximately, inversely proportional to μ. Therefore, we shall simulate the SKR for different values of the mean photon pair of the central channel and find an optimal operation.

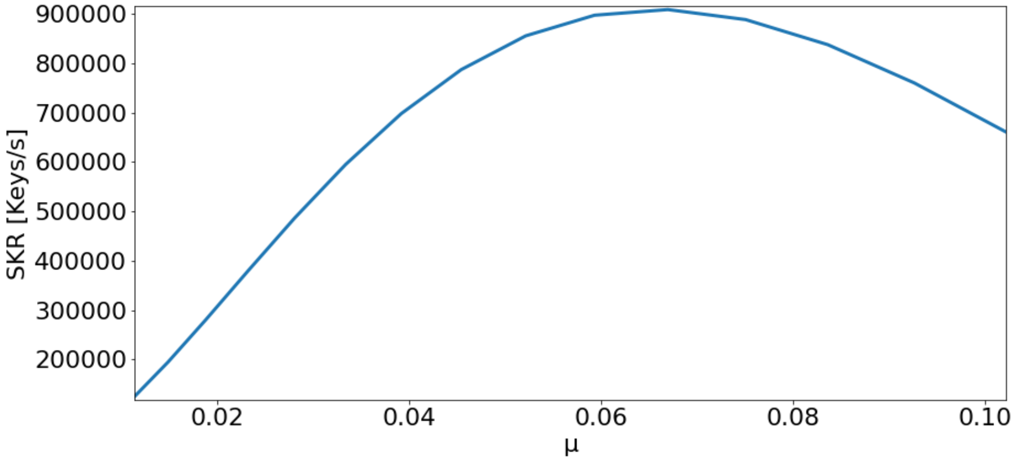

Figure 4.18: The secret key rate for different values for the mean number of pairs generated by the central channel. The distance d was fixed at 100 km.

Using the same assumptions for the efficiencies and a 100 km distance link, we calculate the secret key rate for different values of μ, figure 4.18. We obtain the optimal μ for best performance sharing keys from this figure, which is $\mu_{opt} = 0.067$.

4.5
Entanglement Swapping with Multiple Channels

Now that we implemented our source on a QKD protocol and improved the parameter to get the best SKR of the filtered JSA, we can use this developed source on a more versatile protocol, entanglement swapping, which allows entanglement distribution. For better understanding, figure 4.19 illustrates the setup which we are simulating.

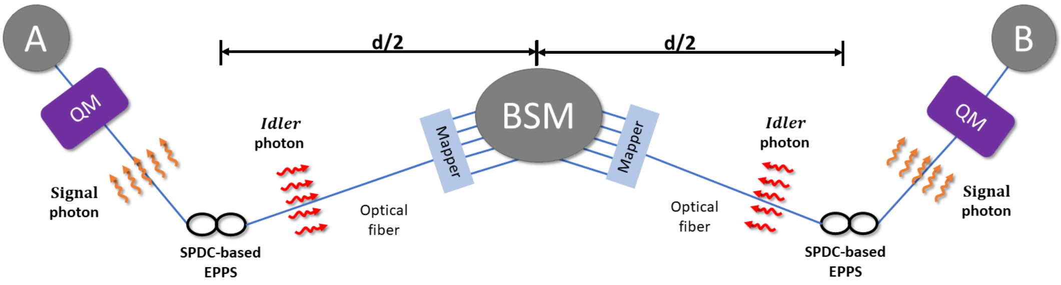

Figure 4.19: Setup for the entanglement swapping with multiple channels.

The idea of the system follows the one presented in section 2.5, but we added the quantum memories and the mapper to map frequency modes into spatial modes going to different detectors. Here, we considered atomic frequency comb (AFC) quantum memories because this allows preparing a frequency selective QM matching our channels [80]. As explained at the begging of this chapter, we chose the wavelengths to match the specification for the memories used in [27] and the low loss on optical fibers. Furthermore, the Filtered SPDC EPPSs are close to the QM to the end nodes A and B, so these distances are negligible compared to d.

To analyze the performance and compare it to the previous setups, we shall use the entanglement swapping to implement BBM92 and measure the secret key rate. Following the same paths as before, we shall define the probability of at least one mode being successful (P_{ab}), which comes from the chance of having no detections. Therefore, first, we calculate the probability of a specific mode m not originating a detection:

$$P_m = 1 - \left[p_m(n > 0)\eta_{det}\eta_{map}\eta_{QM}\right]^2 \eta_{BSM} \tag{4-28}$$

Where $p_m(n > 0)$ is the probability of the mth mode producing one or more pairs, which we defined by eq. 3. The efficiencies are denoted by η, and the subscripts, BSM, det, map, and QM stand for, Bells State measurement, detection, mapper, and quantum memory, respectively. The terms are squared because we have it two times on the setup. As done before, with P_m, one can define P_{ab} as follows.

$$P_{ab} = 1 - \prod_{m=1}^{M} 1 - \left[p_m(n > 0)\eta_{det}\eta_{map}\eta_{QM}\right]^2 \eta_{BSM} \tag{4-29}$$

Moving on to the next step, we shall calculate the ratio of secret keys and qubits received by A and B. Here, we are using the identical approximation as before, assuming the lower bound with the weighted average of secret keys per qubit received, [E]. However, the addition of the BSM and QM affects the QBER, thus, changing the E_m. Therefore, we must, first, calculateMoving on to the next step, we shall calculate the ratio of secret keys and qubits received by A and B. Here, we are using the identical approximation as before, assuming the lower bound with the weighted average of secret keys per qubit received, [E]. However, the addition of the BSM and QM affects the QBER, thus, changing the E_m. Therefore, we must, first, calculate overall visibility, as defined in [17].

$$V_m = (V_m V_{QM} V_{map})^2 V_{BSM} \tag{4-30}$$

Where V_m, V_{QM}, V_{map} and V_{BSM} are the visibilities for the source, quantum memory, mapper, and BSM, respectively. The source visibility follows equation 3-34. Besides, in equation 4-30, the visibilities are squared due to the number of those elements on the setup. The other terms one can obtain by the fidelities using equation 4-31, which comes from the Werner states described in section 3.5. The fidelities and the efficiencies for the simulations, we got from the article [17]. Moreover, in table 4.1, we indicate the values we are using.

$$V_j = \frac{4F_j - 1}{3} \text{ , for } j = \text{BSM, QM and map} \tag{4-31}$$

Parameters from [17]	
F_{QM}	0.968
F_{BSM}	0.972
F_{map}	0.97
η_{BSM}	0.5
η_{QM}	0.4

Table 4.1: Summarizing the values for the fidelities and efficiencies used on the further calculations. F_{QM},F_{BSM}, and F_{map} are the fidelities for the quantum memory, Bell state measurement, and mapper (referred to in the article as feed-forward spectral mode-mapping), respectively. η_{BSM} stands for the Bell state measurement efficiency and η_{QM} for the quantum memory efficiency.

Now, with the visibilities in hand, we can use equation 3-39 to calculate the QBER. Thus, we implement these values on the equation of the Shor-Preskil bound for each channel, obtaining E_m. Furthermore, as in the previous section, we use the average secret key per qubit weighted on the chance of success of a single mode. However, since we are using two sources, the probabilities are squared.

$$[E] = \sum_{m=1}^{M} p(m)^2 E_m \tag{4-32}$$

Finally, coupling equations 4-29 and 4-32 and assuming the pump rate calculated in section 4.3, we can calculate the secret key rate for the BBM92 over the entanglement swapping setup. Figure 4.20 shows the result of this simulation for different distances, d.

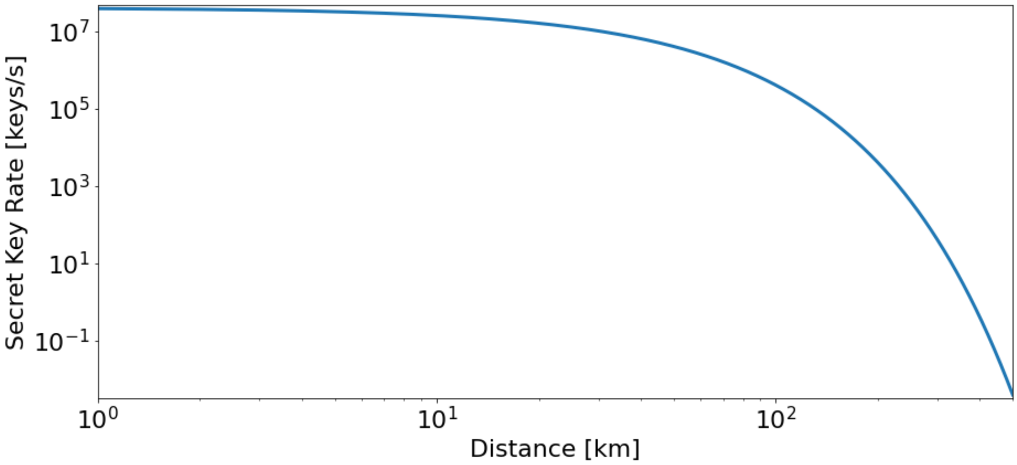

Figure 4.20: Secret key rate over distance for the entanglement swapping setup described before using the filtered source developed in the last section. The efficiencies are detailed in the text.

5
Conclusion and future works

The simulation of the SPDC-based source provides us with a tool to manipulate parameters and extract their effect on the process. Using the knowledge described in chapters 2 and 3, we developed this compact class presented in appendix A. We implemented the program in different scenarios to obtain the results for the last chapter. Using these outcomes, we were able to improve the performance of the source. Figure 5.1 shows the comparison of the SKR for the direct transmission (considering the efficiency of the detectors) and the 26 channels using the filtered SPDC source.

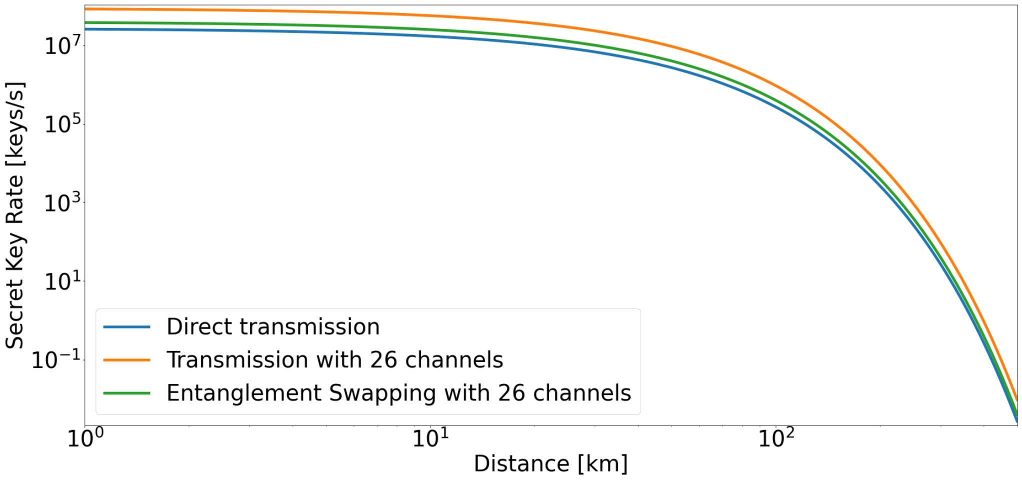

Figure 5.1: Secret key rate for the three different setups discussed before using the source developed and optimized in this work. Therefore, we used managed the pump to produce a maximum average number of pairs of 0.067 and a pulse rate of 3.8 GHz.

Using the values we acquired from the optimization of the source performance, we observe that the filtered SPDC secret key rate is four times greater than the direct transmission. Thus, we obtained a 6 dB improvement using the 26 channels setup. Nonetheless, there is still room for improvement since we are considering the lower bound for the calculations of the SKR.

Now, comparing the entanglement swapping with 26 channels performance with just one multimode source, we observe that this application degrades the SKR. Indeed, we expected this since we are adding other imperfect devices, thus reducing the overall efficiencies and visibilities. However, the entanglement swapping setup is a robust protocol that allows two parties not just to share a secret key but entanglement. Therefore, one can implement this system in different applications, more than just QKD, e.g., quantum repeater and distributed quantum computing. This generality makes our work more notable since these implementations are the core of the future of quantum internet.

Moreover, we are willing to use the simulation developed here to extract results and use them as inputs to other programs more focused on protocols, e.g., Netsquid [81]. Therefore, not relying only on the lower bound approximations but having a more accurate and robust simulation. Besides, we can implement more complexities to the problem and analyze other effects on the physical layer, e.g., dispersion. To improve the simulations, we can implement the equations for a cavity SPDC, making the bandwidth and channel separation control more complex than the presented in this work but more accurate and feasible.

Therefore, we conclude this work by developing a preliminary tool for simulating SPDC sources frequency multiplexed channels. Although we still have some lapidary to do, we could show its utility by optimizing the parameters of the source and applying them to three different setups.

Bibliography

[1] S. Weinberg, *Foundations of Modern Physics*. Cambridge University Press, 2021.

[2] C. Cohen-Tannoudji, B. Diu, and F. Laloë, *Quantum Mechanics*. John Wiley & sons, 2005, vol. 1.

[3] A. Einstein, B. Podolsky, and N. Rosen, “Can quantum-mechanical description of physical reality be considered complete?” *Physical Review*, vol. 47, 1935.

[4] R. H. Brown and R. Twiss, “Correlation between photons in two coherent beams of light,” *Nature*, vol. 177, 1956.

[5] C. K. Hong, Z. Y. Ou, and L. Mandel, “Measurement of subpicosecond time intervals between two photons by interference,” *Phys. Rev. Lett.*, vol. 59, pp. 2044–2046, Nov 1987. [Online]. Available: https://link.aps.org/doi/10.1103/PhysRevLett.59.2044

[6] P. Benioff, “The computer as a physical system: A microscopic quantum mechanical hamiltonian model of computers as represented by turing machines,” *J Stat Phys*, vol. 22, 1980.

[7] P. Shor, “Algorithms for quantum computation: discrete logarithms and factoring,” in *Proceedings 35th Annual Symposium on Foundations of Computer Science*, 1994, pp. 124–134.

[8] J. Preskill, “Quantum computing in the nisq era and beyond,” *Quantum*, vol. 2, p. 79, Aug 2018. [Online]. Available: http://dx.doi.org/10.22331/q-2018-08-06-79

[9] H. Buhrman and H. Röhrig, “Distributed quantum computing,” in *Mathematical Foundations of Computer Science 2003*, B. Rovan and P. Vojtáš, Eds. Berlin, Heidelberg: Springer Berlin Heidelberg, 2003, pp. 1–20.

[10] R. Van Meter and S. J. Devitt, “The path to scalable distributed quantum computing,” *Computer*, vol. 49, no. 9, pp. 31–42, 2016.

[11] A. S. Cacciapuoti, M. Caleffi, F. Tafuri, F. S. Cataliotti, S. Gherardini, and G. Bianchi, “Quantum internet: Networking challenges in distributed quantum computing,” *IEEE Network*, vol. 34, no. 1, pp. 137–143, 2020.

[12] S. Daiss, S. Langenfeld, S. Welte, E. Distante, P. Thomas, L. Hartung, O. Morin, and G. Rempe, "A quantum-logic gate between distant quantum-network modules," *Science*, vol. 371, no. 6529, pp. 614–617, 2021. [Online]. Available: https://www.science.org/doi/abs/10.1126/science.abe3150

[13] C. H. Bennett, G. Brassard, C. Crépeau, R. Jozsa, A. Peres, and W. K. Wootters, "Teleporting an unknown quantum state via dual classical and einstein-podolsky-rosen channels," *Phys. Rev. Lett.*, vol. 70, pp. 1895–1899, Mar 1993. [Online]. Available: https://link.aps.org/doi/10.1103/PhysRevLett.70.1895

[14] H. Kimble, "The quantum internet," *Nature*, vol. 453, pp. 1023–1030, 2008.

[15] C. Simon, "Towards a global quantum network," *Nature Photon*, vol. 11, pp. 678–680, 2017.

[16] K. Chakraborty, D. Elkouss, B. Rijsman, and S. Wehner, "Entanglement distribution in a quantum network: A multicommodity flow-based approach," *IEEE Transactions on Quantum Engineering*, vol. 1, pp. 1–21, 2020.

[17] K. C. Mohsen Falamarzi Askarani and G. C. do Amaral, "Entanglement distribution in multi-platform buffered-router-assisted frequency-multiplexed automated repeater chains," *New Journal of Physics*, vol. 23, 2021.

[18] G. P. Agrawal, *Fiber-Optic Communication Systems*. Willey, 1992.

[19] N. Sangouard, C. Simon, H. de Riedmatten, and N. Gisin, "Quantum repeaters based on atomic ensembles and linear optics," *Rev. Mod. Phys.*, vol. 83, pp. 33–80, Mar 2011. [Online]. Available: https://link.aps.org/doi/10.1103/RevModPhys.83.33

[20] J. L. Park, "The concept of transition in quantum mechanics," *Found Phys*, vol. 1, 1970.

[21] J.-W. Pan, D. Bouwmeester, H. Weinfurter, and A. Zeilinger, "Experimental entanglement swapping: Entangling photons that never interacted," *Phys. Rev. Lett.*, vol. 80, pp. 3891–3894, May 1998. [Online]. Available: https://link.aps.org/doi/10.1103/PhysRevLett.80.3891

[22] H. de Riedmatten, I. Marcikic, J. A. W. van Houwelingen, W. Tittel, H. Zbinden, and N. Gisin, "Long-distance entanglement swapping with photons from separated sources," *Phys. Rev. A*, vol. 71, p. 050302, May 2005. [Online]. Available: https://link.aps.org/doi/10.1103/PhysRevA.71.050302

[23] C. Simon, M. Afzelius, J. Appel *et al.*, "Quantum memories," *The European Physical Journal D*, vol. 58, 2010.

[24] P.-C. Wang, O. Pietx-Casas, M. F. Askarani, and G. C. do Amaral, "Proposal and proof-of-principle demonstration of fast-switching broadband frequency shifting for a frequency-multiplexed quantum repeater," *J. Opt. Soc. Am. B*, vol. 38, no. 4, pp. 1140–1146, Apr 2021. [Online]. Available: http://opg.optica.org/josab/abstract.cfm?URI=josab-38-4-1140

[25] H.-J. Briegel, W. Dür, J. I. Cirac, and P. Zoller, "Quantum repeaters: The role of imperfect local operations in quantum communication," *Phys. Rev. Lett.*, vol. 81, pp. 5932–5935, Dec 1998. [Online]. Available: https://link.aps.org/doi/10.1103/PhysRevLett.81.5932

[26] L. Duan, M. Lukin, J. Cirac, and P. Zoller, "Long-distance quantum communication with atomic ensembles and linear optics," *Nature*, vol. 414, 2001.

[27] M. I. G. Puigibert, M. F. Askarani, J. H. Davidson, V. B. Verma, M. D. Shaw, S. W. Nam, T. Lutz, G. C. Amaral, D. Oblak, and W. Tittel, "Entanglement and nonlocality between disparate solid-state quantum memories mediated by photons," *Phys. Rev. Research*, vol. 2, p. 013039, Jan 2020. [Online]. Available: https://link.aps.org/doi/10.1103/PhysRevResearch.2.013039

[28] M. F. Askarani, A. Das, J. H. Davidson, G. C. Amaral, N. Sinclair, J. A. Slater, S. Marzban, C. W. Thiel, R. L. Cone, D. Oblak, and W. Tittel, "Long-lived solid-state optical memory for high-rate quantum repeaters," *Phys. Rev. Lett.*, vol. 127, p. 220502, Nov 2021. [Online]. Available: https://link.aps.org/doi/10.1103/PhysRevLett.127.220502

[29] G. Keiser, *Optical Fiber Communications*. McGraw-Hill, 1983.

[30] J. Calsamiglia and N. Lütkenhaus, "Maximum efficiency of a linear-optical bell-state analyzer," *Applied Physics B*, vol. 72, 2001.

[31] A. Holevo, "Information-theoretical aspects of quantum measurement," *Probl. Peredachi Inf.*, vol. 9, 1973.

[32] J. Preskill, "Quantum computing and the entanglement frontier," 2012. [Online]. Available: https://arxiv.org/abs/1203.5813

[33] R. P. Feynman, "Simulating physics with computers," *Int J Theor Phys*, vol. 21, 1982.

[34] R. de Wolf, "The potential impact of quantum computers on society," *Ethics and Information Technology*, vol. 19, pp. 271–276, 2017.

[35] D. E. Denning, "Is quantum computing a cybersecurity threat? although quantum computers currently don't have enough processing power to break encryption keys, future versions might." *American Scientist*, vol. 107, 2019.

[36] Y. Wang, H. Zhang, and H. Wang, "Quantum polynomial-time fixed-point attack for rsa," *China Communications*, vol. 15, no. 2, pp. 25–32, 2018.

[37] V. Bhatia and K. Ramkumar, "An efficient quantum computing technique for cracking rsa using shor's algorithm," in *2020 IEEE 5th International Conference on Computing Communication and Automation (ICCCA)*, 2020, pp. 89–94.

[38] C. H. Bennett and G. Brassard, "Quantum cryptography: Public key distribution and coin tossing," in *the IEEE International Conference on Computers, Systems and Signal Processing*, Banglore, India, 1984.

[39] N. Gisin and R. Thew, "Quantum communication," *Nature Photon*, vol. 1, p. 165–171, 2007.

[40] P. W. Shor and J. Preskill, "Simple proof of security of the bb84 quantum key distribution protocol," *Phys. Rev. Lett.*, vol. 85, pp. 441–444, Jul 2000. [Online]. Available: https://link.aps.org/doi/10.1103/PhysRevLett.85.441

[41] A. K. Ekert, "Quantum cryptography based on bell's theorem," *Phys. Rev. Lett.*, vol. 67, pp. 661–663, Aug 1991. [Online]. Available: https://link.aps.org/doi/10.1103/PhysRevLett.67.661

[42] C. H. Bennett, G. Brassard, and N. D. Mermin, "Quantum cryptography without bell's theorem," *Phys. Rev. Lett.*, vol. 68, pp. 557–559, Feb 1992. [Online]. Available: https://link.aps.org/doi/10.1103/PhysRevLett.68.557

[43] P. Jouguet and S. Kunz-Jacques, "High performance error correction for quantum key distribution using polar codes," *Quantum Information and Computation*, vol. 14, no. 3–4, p. 329–338, mar 2014.

[44] Y. Watanabe, "Privacy amplification for quantum key distribution," *Journal of Physics A: Mathematical and Theoretical*, vol. 40, no. 3, pp. F99–F104, dec 2006. [Online]. Available: https://doi.org/10.1088/1751-8113/40/3/f03

[45] R. Chatterjee, K. Joarder, S. Chatterjee, B. C. Sanders, and U. Sinha, "qkdsim, a simulation toolkit for quantum key distribution including imperfections: Performance analysis and demonstration of the b92 protocol using heralded photons," *Phys.*

Rev. Applied, vol. 14, p. 024036, Aug 2020. [Online]. Available: https://link.aps.org/doi/10.1103/PhysRevApplied.14.024036

[46] W. J. Munro, K. Azuma, K. Tamaki, and K. Nemoto, "Inside quantum repeaters," *IEEE Journal of Selected Topics in Quantum Electronics*, vol. 21, no. 3, pp. 78–90, 2015.

[47] J. A. Armstrong, N. Bloembergen, J. Ducuing, and P. S. Pershan, "Interactions between light waves in a nonlinear dielectric," *Phys. Rev.*, vol. 127, pp. 1918–1939, Sep 1962. [Online]. Available: https://link.aps.org/doi/10.1103/PhysRev.127.1918

[48] P. A. Franken and J. F. Ward, "Optical harmonics and nonlinear phenomena," *Rev. Mod. Phys.*, vol. 35, pp. 23–39, Jan 1963. [Online]. Available: https://link.aps.org/doi/10.1103/RevModPhys.35.23

[49] D. Huber, M. Reindl, J. Aberl, A. Rastelli, and R. Trotta, "Semiconductor quantum dots as an ideal source of polarization-entangled photon pairs on-demand: a review," *Journal of Optics*, vol. 20, no. 7, p. 073002, jun 2018. [Online]. Available: https://doi.org/10.1088/2040-8986/aac4c4

[50] D. D. B. Rao, S. Yang, and J. Wrachtrup, "Generation of entangled photon strings using nv centers in diamond," *Phys. Rev. B*, vol. 92, p. 081301, Aug 2015. [Online]. Available: https://link.aps.org/doi/10.1103/PhysRevB.92.081301

[51] G. Jabir, M.V.and Samanta, "Robust, high brightness, degenerate entangled photon source at room temperature," *Sci Rep*, vol. 7, 2017.

[52] *SPDC810 Spontaneous Parametric Down-Conversion Source*, ThorLabs, 2020.

[53] *Benchtop Polarization-entangled Photon Sources: Ruby & Emerald*, OZ Optics, 2022.

[54] C.-G. Shu, X. Xin, Y.-M. Liu, Z.-Y. Yu, W.-J. Yao, D.-L. Wang, and G. Cao, "The mechanism of producing energy-polarization entangled photon pairs in the cavity-quantum electrodynamics scheme," *Chinese Physics B*, vol. 21, no. 4, p. 044208, apr 2012. [Online]. Available: https://doi.org/10.1088/1674-1056/21/4/044208

[55] T. Chakraborty, H. van Brug, A. Das, O. Pietx-Casas, P.-C. Wang, G. C. d. Amaral, A. L. Tchebotareva, and W. Tittel, "Frequency multiplexed photon

pairs and detection for quantum repeaters," 2022. [Online]. Available: https://arxiv.org/abs/2205.10028

[56] A. Khalique and B. C. Sanders, "Practical long-distance quantum key distribution through concatenated entanglement swapping with parametric down-conversion sources," *J. Opt. Soc. Am. B*, vol. 32, no. 11, pp. 2382–2390, Nov 2015. [Online]. Available: http://opg.optica.org/josab/abstract.cfm?URI=josab-32-11-2382

[57] C. Gerry and P. Knight, *Introductory Quantum Optics*. Cambridge University Press, 2005.

[58] J. F. Clauser, M. A. Horne, A. Shimony, and R. A. Holt, "Proposed experiment to test local hidden-variable theories," *Physical Review Letters*, vol. 23, pp. 880–884, 1969.

[59] W. Tittel, J. Brendel, H. Zbinden, and N. Gisin, "Violation of bell inequalities by photons more than 10 km apart," *Physical Review Letter*, vol. 81, pp. 3563–3566, 1998.

[60] Y.-H. Kim, S. P. Kulik, and Y. Shih, "Quantum teleportation of a polarization state with a complete bell state measurement," *Phys. Rev. Lett.*, vol. 86, pp. 1370–1373, Feb 2001. [Online]. Available: https://link.aps.org/doi/10.1103/PhysRevLett.86.1370

[61] R. W. Boyd, *Nonlinear Optics*, 3rd ed. Academic Press, 2008.

[62] W. P. Grice and I. A. Walmsley, "Spectral information and distinguishability in type-ii down-conversion with a broadband pump," *Phys. Rev. A*, vol. 56, pp. 1627–1634, Aug 1997. [Online]. Available: https://link.aps.org/doi/10.1103/PhysRevA.56.1627

[63] F. J. Dyson, "The radiation theories of tomonaga, schwinger, and feynman," *Physical Review*, vol. 75, pp. 486–502, 1949.

[64] P. M. Leung, W. J. Munro, K. Nemoto, and T. C. Ralph, "Spectral effects of strong $\chi^{(2)}$ nonlinearity for quantum processing," *Phys. Rev. A*, vol. 79, p. 042307, Apr 2009. [Online]. Available: https://link.aps.org/doi/10.1103/PhysRevA.79.042307

[65] F. Laudenbach, H. Hübel, M. Hentschel, P. Walther, and A. Poppe, "Modelling parametric down-conversion yielding spectrally pure photon pairs," *Optics Express*, vol. 24, p. 2712–2727, 2016.

[66] A. M. Brańczyk, T. C. Ralph, W. Helwig, and C. Silberhorn, "Optimized generation of heralded fock states using parametric down-conversion," *New Journal of Physics*, vol. 12, no. 6, p. 063001, jun 2010. [Online]. Available: https://doi.org/10.1088/1367-2630/12/6/063001

[67] P. R. Tapster and J. G. Rarity, "Photon statistics of pulsed parametric light," *Journal of Modern Optics*, vol. 45, no. 3, pp. 595–604, 1998. [Online]. Available: https://doi.org/10.1080/09500349808231917

[68] A. Christ, K. Laiho, A. Eckstein, K. N. Cassemiro, and C. Silberhorn, "Probing multimode squeezing with correlation functions," *New Journal of Physics*, vol. 13, no. 3, p. 033027, mar 2011. [Online]. Available: https://doi.org/10.1088/1367-2630/13/3/033027

[69] A. Peres, "Separability criterion for density matrices," *Phys. Rev. Lett.*, vol. 77, pp. 1413–1415, Aug 1996. [Online]. Available: https://link.aps.org/doi/10.1103/PhysRevLett.77.1413

[70] I. Marcikic, H. de Riedmatten, W. Tittel, H. Zbinden, M. Legré, and N. Gisin, "Distribution of time-bin entangled qubits over 50 km of optical fiber," *Phys. Rev. Lett.*, vol. 93, p. 180502, Oct 2004. [Online]. Available: https://link.aps.org/doi/10.1103/PhysRevLett.93.180502

[71] R. F. Werner, "Quantum states with einstein-podolsky-rosen correlations admitting a hidden-variable model," *Phys. Rev. A*, vol. 40, pp. 4277–4281, Oct 1989. [Online]. Available: https://link.aps.org/doi/10.1103/PhysRevA.40.4277

[72] N. Gisin, G. Ribordy, W. Tittel, and H. Zbinden, "Quantum cryptography," *Rev. Mod. Phys.*, vol. 74, pp. 145–195, Mar 2002. [Online]. Available: https://link.aps.org/doi/10.1103/RevModPhys.74.145

[73] C. E. Shannon, "A mathematical theory of communication," *The Bell System Technical Journal*, vol. 27, no. 3, pp. 379–423, 1948.

[74] R. Schiek and T. Pertsch, "Absolute measurement of the quadratic nonlinear susceptibility of lithium niobate in waveguides," *Opt. Mater. Express*, vol. 2, no. 2, pp. 126–139, Feb 2012. [Online]. Available: http://opg.optica.org/ome/abstract.cfm?URI=ome-2-2-126

[75] D. H. Jundt, "Temperature-dependent sellmeier equation for the index of refraction, ne, in congruent lithium niobate," *Optics Letters*, vol. 22, no. 20, pp. 1553–1555, October 1997.

[76] F. Pignatiello, M. D. Rosa, P. Ferraro, S. Grilli, P. D. Natale, A. Arie, and S. D. Nicola, “Measurement of the thermal expansion coefficients of ferroelectric crystals by a moire’ interferometer,” *Optics Communications*, vol. 277, p. 14–18, 2007.

[77] G. B. Arfken and H. J. Weber, *Mathematical Methods for Physicists*, 6th ed. Academic Press, 2005.

[78] O. Pietx-Casas, G. C. d. Amaral, T. Chakraborty, R. Berrevoets, T. Middelburg, J. A. Slater, and W. Tittel, “Spectrally multiplexed hong-ou-mandel interference,” 2021. [Online]. Available: https://arxiv.org/abs/2111.13610

[79] Z. Xie, T. Zhong, S. Shrestha *et al.*, “Harnessing high-dimensional hyperentanglement through a biphoton frequency comb,” *Nature Photon*, vol. 9, pp. 536–542, 2015.

[80] M. F. Askarani, T. Lutz, M. G. Puigibert, N. Sinclair, D. Oblak, and W. Tittel, “Persistent atomic frequency comb based on zeeman sub-levels of an erbium-doped crystal waveguide,” *J. Opt. Soc. Am. B*, vol. 37, no. 2, pp. 352–358, Feb 2020. [Online]. Available: http://opg.optica.org/josab/abstract.cfm?URI=josab-37-2-352

[81] T. Coopmans, R. Knegjens, A. Dahlberg *et al.*, “Netsquid, a network simulator for quantum information using discrete events,” *Communications Physics*, vol. 4, 2021.

A
Codes

```
from numba import jit
import numpy as np
import matplotlib.pyplot as plt

# Basic function to use jit

@jit(nopython=True, parallel = True,fastmath = True)
def MatrixProd(A,B):
    return A*B
@jit(nopython=True,fastmath = True)
def power(a,n):
    return np.power(a,n)

@jit(nopython=True, parallel = True,fastmath = True)
def Sum (x):
    return np.sum(x)

def H(Q): return -Q*np.log2(Q)-(1-Q)*np.log2(1-Q)

class LN_Crystal:
    def __init__(self,TempK = 313,Polper = 7, L = 15e3):
        self.T = TempK-273
        self.Polper = Polper
        self.L = L

        #index
        self.a = [5.35583,0.100473,0.20692,100,11.34927,1.5334E-2]
        self.b = [4.629E-7,3.862E-8,-0.89E-8,2.657E-5]
        self.f = (self.T-24.5)*(self.T+570.82)
        self.term1 = self.a[0];
        self.term2 = self.b[0]*self.f;
        #polper
        alpha = [(3.4)*1E-6,(-1)*1E-9]
        T0        = 25
        f0        = 1/Polper
        sin_beta0 = (-1) * 1/Polper
        F0        = 2*sin_beta0
        F_T       = F0 + 2*f0*(alpha[0]*(self.T-T0) + alpha[1]*power(
                                                            self.T-T0,2))
        sin_beta      = F_T/2
        self.polingPeriod = power((-1)*sin_beta,-1)
        self.check = (F_T - F0)*1e-3

    def indexTemp(self,wavelength):
        a = self.a
        b = self.b
        f = self.f
        term3 = (a[1] + b[1]*f)/(power(wavelength,2) - power(a[2] +
                                                            b[2]*f,2))
        term4 = (a[3] + b[3]*f)/(power(wavelength,2) - power(a[4],2))
        term5 = a[5]*np.power(wavelength,2)

        return np.sqrt(self.term1 + self.term2 + term3
                       + term4 - term5)

class KTP_Crystal:
    def __init__(self,TempK = 313,Polper = 7, L = 15e3):
        self.T = TempK-273
        self.Polper = Polper
        self.L = L

        #polper
        alpha = [(3.4)*1E-6,(-1)*1E-9]
        T0        = 25
        f0        = 1/Polper
        sin_beta0 = (-1) * 1/Polper
        F0        = 2*sin_beta0
        F_T       = F0 + 2*f0*(alpha[0]*(self.T-T0) + alpha[1]*
                              power(self.T-T0,2))
        sin_beta  = F_T/2
        self.polingPeriod = power((-1)*sin_beta,-1)
        self.check = (F_T - F0)*1e-3

    def indexTemp(self,wavelength):

        return np.sqrt(1.94460+1.617*wavelength**2/
                       (wavelength**2-0.047)-0.0149*wavelength**2)



class EPPS:
    def __init__(self,Crystal='LN',Numpoints=1000,c=3e8,
                 eps=8.854*1e-12,xi_2=20.6*1e-12,tw=50e-12,R=100e6,
                 peakPower=1,diam=4.1*1e-6,pumpWave=0.5235,
                 idlerRange=[1.527,1.533],
                 integral_range=[1.527,1.533],TempK=313,Polper=7,L=15e3):

        self.Numpoints = Numpoints
        self.pumpWave = pumpWave

        if Crystal == 'LN':
            self.crystal = LN_Crystal(TempK=TempK,Polper=Polper,L=L)
        elif Crystal == 'KTP':
            self.crystal = KTP_Crystal(TempK=TempK,Polper=Polper,L=L)
        else:
            self.crystal = LN_Crystal(TempK=TempK,Polper=Polper,L=L)

        sig_t = tw/(2*np.sqrt(np.log(2)))

        self.idlerWave = np.linspace(idlerRange[0],idlerRange[1],
                                     Numpoints)
        self.signalWave = np.float_power(1/pumpWave -
                                         1./self.idlerWave,-1)
        self.Idler,self.Signal = np.meshgrid(self.idlerWave,
                                             self.signalWave)

        # Amplitude
        hbar = 1.054571*1e-34 #J/s
        indp = self.crystal.indexTemp(pumpWave)
        self.modeArea = np.pi*diam**2/4
        self.averagePower = R*tw*peakPower/0.94
        self.I = self.averagePower/(self.modeArea)
        self.E = power(2*self.I/(c*eps*indp),1/2)
        self.Xi = 2*np.pi*xi_2*L*1e-6*self.modeArea*self.E*eps/(
            hbar*1j)

        # Mu calculation - Energy conservation
        Fs = c*1e6/self.Signal
        Fi = c*1e6/self.Idler
        F = Fs+Fi
        F0 = c/pumpWave*1e6
        self.Alpha = np.exp(-2*power(np.pi*sig_t*(F-F0),2))

        # Phi Calculation - Momentum conservation
        indi = self.crystal.indexTemp(self.Idler)
        inds = self.crystal.indexTemp(self.Signal)

        kp = 2*np.pi*indp/pumpWave
        ki = 2*np.pi*indi/self.Idler
        ks = 2*np.pi*inds/self.Signal

        Dk = 2*np.pi/self.crystal.polingPeriod
        Dkm = (kp-ki-ks-Dk)

        self.PSI = MatrixProd(np.exp(1j*Dkm*L/2),np.sin(Dkm*L/2)/(
            Dkm*L/2))

        # Joint spectral amplitude and intensity
        self.JSA_mod = MatrixProd(self.Alpha,self.PSI)
        self.JSI_mod = power(np.absolute(MatrixProd(self.Alpha,
                                                    self.PSI)),2)

        Nf = self.Normalization(Numpoints=Numpoints,c=c,
                                idlerRange=integral_range,
                                pumpWave=pumpWave,L=L,tw=tw)

        self.JSA_mod = Nf*self.JSA_mod
        self.JSI_mod = Nf**2*self.JSI_mod
```

```
        self.JSA = self.Xi*self.JSA_mod
        self.JSI = np.absolute(self.Xi)**2*self.JSI_mod

    def Normalization (self,Numpoints=1000,c=3e8,
                       idlerRange=[1.527,1.533],
                       pumpWave=0.5235,L=10e-3,tw=50e-12):

        sig_t = tw/(2*np.sqrt(np.log(4)))

        idlerWave = np.linspace(idlerRange[0],idlerRange[1],
                                Numpoints)
        signalWave = np.float_power(1/pumpWave - 1./idlerWave,-1)
        Idler,Signal = np.meshgrid(idlerWave,signalWave)

        # Mu calculation - Energy conservation
        Fs = c*1e6/Signal
        Fi = c*1e6/Idler
        F = Fs+Fi
        F0 = c/pumpWave*1e6
        Alpha = np.exp(-2*power(np.pi*sig_t*(F-F0),2))

        # Phi Calculation - Momentum conservation
        indp = self.crystal.indexTemp(pumpWave)
        indi = self.crystal.indexTemp(Idler)
        inds = self.crystal.indexTemp(Signal)

        kp = 2*np.pi*indp/pumpWave
        ki = 2*np.pi*indi/Idler
        ks = 2*np.pi*inds/Signal

        Dk = 2*np.pi/self.crystal.polingPeriod
        Dkm = (kp-ki-ks-Dk)

        PSI = MatrixProd(np.exp(1j*Dkm*L/2),np.sin(Dkm*L/2)/(
                                                        Dkm*L/2))

        # Joint spectral amplitude and intensity
        JSI_mod = power(np.absolute(MatrixProd(Alpha,PSI)),2)
        self.Nf = power(np.trapz(-np.trapz(JSI_mod,x=idlerWave),
                                                        x=signalWave),-1/2)

        return self.Nf

    def Filter (self,c=3e8,name='idler',lamb0=1.531,band=1e9):
        dl = lamb0**2*band/(c*1e6)
        sig = dl/(2*np.sqrt(np.log(2)))

        if name == 'idler':
            return np.exp(-(self.idlerWave-lamb0)**2/(2*sig**2))

        else:
            return np.exp(-(self.signalWave-lamb0)**2/(2*sig**2))

    def Filtering (self,fcenter_idler = 1.5305,band_idler=100e6,
                   fcenter_signal=0.7957,band_signal=100e6):

        idlerFilter = self.Filter(name='idler',
                                  lamb0=fcenter_idler,
                                  band=band_idler)
        signalFilter = self.Filter(name='signal',
                                   lamb0=fcenter_signal,
                                   band=band_signal)
        signalFilter.resize(signalFilter.size,1)
        self.FJSA = idlerFilter*self.JSA*signalFilter
        self.FJSI = power(np.absolute(self.FJSA),2)


    def Multiple_filters (self,Nfilters = 1,
                          fcenter_idler = np.array([1.5305]),
                          band_idler=10e6,band_signal=10e6):

        fcenter_signal = 1/(1/0.5235-1/fcenter_idler)
        idlerFilter = self.Filter(name='idler',
                                  lamb0=fcenter_idler[0],
                                  band=band_idler)
        signalFilter = self.Filter(name='signal',
                                   lamb0=fcenter_signal[0],
                                   band=band_signal)

        for i in list(range(1,Nfilters)):
            idlerFilter = idlerFilter + self.Filter(name='idler',
                                                    lamb0=fcenter_idler[i],
                                                    band=band_idler)
            signalFilter = signalFilter + self.Filter(name='signal',
                                                      lamb0=fcenter_signal[i],
                                                      band=band_signal)

        signalFilter.resize(signalFilter.size,1)
        self.MFJSA = idlerFilter*self.JSA*signalFilter
        self.MFJSI = power(np.absolute(self.MFJSA),2)
        self.idlerFilter = idlerFilter

    def plotJSI (self):
        fig, ax = plt.subplots()
        ax.set(xlabel = 'Idler␣Wavelength␣[nm]',
               ylabel = 'Signal␣Wavelength␣[nm]',
               title = 'Joint␣Spectral␣Intensity')
        ax.invert_yaxis()
        cs = ax.contourf(self.Idler*1e3,
                         self.Signal*1e3,
                         self.JSI,100,
                         cmap='viridis')
        fig.colorbar(cs)
        plt.show()

    def plotFJSI (self):
        fig, ax = plt.subplots()
        ax.set(xlabel = 'Idler␣Wavelength␣[nm]',
               ylabel = 'Signal␣Wavelength␣[nm]',
               title = 'Joint␣Spectral␣Intensity')
        ax.invert_yaxis()
        cs = ax.contourf(self.Idler*1e3,
                         self.Signal*1e3,
                         self.FJSI,100,
                         cmap='viridis')
        fig.colorbar(cs)
        plt.show()

    def plotMFJSI (self):
        fig, ax = plt.subplots()
        ax.set(xlabel = 'Idler␣Wavelength␣[nm]',
               ylabel = 'Signal␣Wavelength␣[nm]',
               title = 'Joint␣Spectral␣Intensity')
        ax.invert_yaxis()
        cs = ax.contourf(self.Idler*1e3,
                         self.Signal*1e3,
                         self.MFJSI,100,
                         cmap='viridis')
        fig.colorbar(cs)
        plt.show()

    def SVD (self, opt = 'normal'):
        # Single value decomposition
        if opt == 'normal':
            self.U, self.r, self.Vt = np.linalg.svd(self.JSA)

        elif opt == 'filtered':
            self.U, self.r, self.Vt = np.linalg.svd(self.FJSA)

        elif opt == 'multi_filtered':
            self.U, self.r, self.Vt = np.linalg.svd(self.MFJSA)

        else :
            print('ERROR!␣Wrong␣option␣(opt).')
            return None

        self.B = np.linalg.norm(self.r)

    def Purity (self):
        lamb = self.r/self.B
        self.P = Sum(np.power(lamb,4))
        return self.P

    def g2cross (self):
        dli = self.idlerWave[1]-self.idlerWave[0]
        dls = -np.power(self.pumpWave/(self.idlerWave-
                                              self.pumpWave),2)*dli

        self.true_B = power(np.sum(self.r**2*np.abs(dli*dls)),1/2)

        r = (self.r/self.B)*np.abs(self.true_B)

        self.g2 =  1 + Sum(power(np.sinh(r),4))/power(Sum(power(
                  np.sinh(r),2)),2) + power(Sum(power(
                  np.sinh(r),2)),-1)
        return self.g2

    def Visibility (self):
        self.V = (self.g2 - 1)/(self.g2 + 1)
        return self.V

    def QBER (self):
        self.Q = (1-self.V)/2
        return self.Q

    def PairRate (self,k):
        self.Rp = 1-(1+k)*H(self.Q)
        return self.Rp
```